



HAL
open science

Restricted optimal paths to transition in a plane Couette flow

Frédéric Alizard, Lionel Le Penven, Anne Cadiou, Bastien Di Pierro, Marc
Buffat

► **To cite this version:**

Frédéric Alizard, Lionel Le Penven, Anne Cadiou, Bastien Di Pierro, Marc Buffat. Restricted optimal paths to transition in a plane Couette flow. *European Journal of Mechanics - B/Fluids*, 2021, 85, pp.261-275. 10.1016/j.euromechflu.2020.10.004 . hal-02972434

HAL Id: hal-02972434

<https://hal.science/hal-02972434>

Submitted on 1 Nov 2020

HAL is a multi-disciplinary open access archive for the deposit and dissemination of scientific research documents, whether they are published or not. The documents may come from teaching and research institutions in France or abroad, or from public or private research centers.

L'archive ouverte pluridisciplinaire **HAL**, est destinée au dépôt et à la diffusion de documents scientifiques de niveau recherche, publiés ou non, émanant des établissements d'enseignement et de recherche français ou étrangers, des laboratoires publics ou privés.

Restricted optimal paths to transition in a plane Couette flow

Frédéric Alizard, Lionel Le Penven, Anne Cadiou, Bastien Di Pierro and Marc Buffat

LMFA, UMR 5509, Univ Lyon, Université Claude Bernard Lyon 1, École Centrale de Lyon, INSA Lyon, CNRS, 43 boulevard du 11 novembre 1918, F-69100, VILLEURBANNE, France.

Abstract

To identify laminar/turbulent transition paths in plane Couette flow, a variational formulation incorporating a restricted nonlinear (RNL) system that retains a single streamwise Fourier mode, is used. Considering the flow geometry originally used by Monokrousos *et al* (*Phys. Rev. Lett.*, vol. 106, 2011, 134502) and Duguet *et al* (*Phys. of Fluids*, vol. 25, 2013, 084103) and the same Reynolds numbers (Re), we show that initial perturbations obtained by RNL optimizations exhibit spatial localization. Two optimal states are found with comparable initial energy levels above which the flow structure evolves to turbulence. It is found that this level is twice that of the minimal threshold energy which has been obtained using the full nonlinear equations (Duguet *et al* *Phys. of Fluids*, vol. 25, 2013, 084103). Especially, the Re dependence of energy thresholds is studied within a RNL optimization framework for the first time, with evidence for a $O(Re^{-2.65})$ scaling close to the one found using the full Navier-Stokes equations $O(Re^{-2.7})$. The first state is obtained for a short target time. It is symmetric with respect to the mid-plane $y = 0$ and spanwise localized. For a long target time, the optimal appears to be localized in both spanwise and wall-normal directions. The mechanisms highlighted within the scope of nonlinear nonmodal theory (Kerswell *Ann. Review of Fluid Mech.*, vol. 50, 2018, 319-345): Orr mechanism, oblique wave interaction, lift-up, streak

*Frédéric Alizard, frederic.alizard@univ-lyon1.fr

breakdown, localized pocket of turbulence and turbulence spreading, are also observed in the RNL simulations. Although greatly simplified, the RNL system provides a good approximation of these different fundamental mechanisms. The analysis gives then some insight into the potential of RNL optimizations for estimating Re scaling laws and routes to turbulence for shear flows.

Keywords: RNL optimisations, subcritical transition.

1. Introduction

Streamwise streaks are elongated regions of defect or excess of streamwise velocity. They play a fundamental role in the laminar-turbulent transition process for all canonical wall-bounded flows (Couette, channel or flat-plate boundary layer flows, Klebanoff (1971); Reddy et al. (1998); Andersson et al. (2001)).
5 Streaks are generated by rolls through the linear lift-up mechanism (Landhal, 1980). This mechanism constitutes a key element to explain transition in subcritical conditions, *i.e.* in the absence of linear modal instability (see for a recent review Brandt (2014)). For parallel flows, nonmodal linear theory has revealed that streamwise invariant streaks are the perturbations which experience
10 the largest transient energy growth (Schmid and Henningson, 2001). However, nonlinearities have a stabilizing effect on the growth of streaks (Joseph, 1976) which is the reason why purely linear optimal modes cannot completely explain subcritical transition.

15 The experiments of Swearingen and Blackwelder (1987) have first shown that streaks may undergo secondary instability, either spanwise symmetric (varicose) or anti-symmetric (sinuous), and subsequently break down into turbulence (Asai et al., 2002; Brandt, 2007; Vaughan and Zaki, 2011; Hack and Zaki, 2014). Then, the determination of the lower bound in kinetic energy threshold for inducing
20 subcritical transition in shear flows and the corresponding Re -scaling laws have been the object of many studies.

A first attempt at establishing the kinetic energy threshold for canonical flows has been carried out by Reddy et al. (1998). These authors have in-

vestigated streak instability considering initial optimal perturbations with the
25 greatest potential for linear transient growth over all possible target times. For
this streamwise vortex (SV) scenario, they have found that the initial kinetic
energy of rolls causing streak breakdown scales as $O(Re^{-2.2})$ for plane Cou-
ette flow (pCf). Similarly, Reddy et al. (1998) have found that the kinetic
energy threshold for transition initiated by a pair of oblique waves (OW) scales
30 as $O(Re^{-2.5})$. These scalings have been refined by Duguet et al. (2010) with
evidence for a $O(Re^{-2})$ scaling for both OW and SV scenarios

More recently, Karp and Cohen (2014, 2017) showed that the onset of sec-
ondary instability is not necessarily correlated with initial condition maximiz-
ing the linear energy growth. The authors have shown that the optimal set of
35 parameters are rather associated with initial disturbances which generate the
strongest inflection point due to nonlinearities. In particular, Karp and Cohen
(2014, 2017) concluded that both the spanwise wavenumber and initial threshold
energy differ from the values based on optimal transient energy growth. Follow-
ing this line of thought, Cossu et al. (2011) explored the streak breakdown in
40 a two-dimensional parameter space consisting to the amplitude of streaks and
their secondary perturbation. Their numerical experiments on subcritical shear
flows illustrate that the maximal energy growth condition is not an essential
criterion for transition. It is rather about whether or not finite-amplitude
disturbances can approach the edge of chaos before being repelled towards the
45 turbulent attractor (Skufca et al., 2006). For parallel flows, the trajectory evol-
ving on the edge of chaos is organized around relative attractors known as edge
states, which are invariant solutions of the Navier-Stokes equations, and their
heteroclinic connections (Duguet et al., 2008).

Invariant solutions also called exact coherent states (ECS) have been found
50 in various shear flows including pCf (Nagata, 1990; Clever and Busse, 1997),
channel flow (Itano and Toh, 2001), pipe flow (Duguet et al., 2008) or boundary
layers (Khapko et al., 2016). For narrow periodic boxes, ECS arise through a
saddle-node bifurcation at some critical Reynolds number $Re = R_s$ (Nagata,
1990). For $Re > R_s$, the ECS separate into upper and lower branches. From

55 a dynamical system point of view, the lower branch solutions are embedded
in the laminar-turbulent boundary and correspond to the edge states. These
solutions share some basic features that are well described by the self-sustaining
process (SSP) (Benney, 1984; Waleffe and Kim, 1997; Waleffe, 2003, 1998):
streamwise vortices induce streaks by lift-up effect and by quadratic interactions
60 of a travelling wave (an unstable eigenmode or a superposition of eigenmodes
of the streak), these streaks in turn regenerate rolls. It should be noted that
the fundamental mechanism enabling the self-sustainment of the vortices is still
a subject of debate (either due to a vortex stretching mechanism, Schoppa and
Hussain (2002) or an advection term, Hamilton et al. (1995)).

65 Within the SSP theory, Waleffe (2003) recovered the Nagata/Clever equilib-
rium state for pCf (Nagata, 1990; Clever and Busse, 1997). DNS of Wang et al.
(2007) illustrated that lower branch states in pCf have an asymptotic struc-
ture that consists of $O(1)$ streaks, streamwise rolls and a superimposed wave
of $O(Re^{-1})$ with negligible higher harmonics. For large Re , the fundamental
70 mode concentrates along the critical layer. However, these pioneering studies
have been carried out in constrained computational boxes that cannot describe
space-time dynamics observed experimentally in large domains (Bottin et al.,
1997). In this context, Schneider et al. (2010); Duguet et al. (2009) first found
edge states in wide and long domains that are localized in spanwise or both
75 spanwise and downstream directions for pCf. For the same flow case, Pershin
et al. (2019) characterized the inherent dynamics of spanwise localized states.
For low Re , they showed that the flow exhibits very long-lived chaotic transient
dynamics before relaminarizing.

This geometrical picture suggests that the estimation of the lower bound in
80 kinetic energy threshold for subcritical shear flows could be improved. Within
this scope, the concept of minimal perturbation, that represents the point where
the distance (for a given norm) between the edge and the basic laminar state is
the shortest, has been introduced by Viswanath and Cvitanovic (2009); Kerswell
(2018). This “minimal seed” has the lowest energy on the edge (noted E_c , here-
85 after) and can only be computed using nonlinear optimization methods. Pringle

and Kerswell (2010); Pringle et al. (2012) conjectured that the minimal seed is associated with the perturbation of initial energy E_0 that experiences the largest energy growth for asymptotically large target time and which is such that for any E_0 exceeding a critical threshold E_c , the optimization problem fails to converge

90 to a smooth solution (*i.e.* a turbulent end state). A picture that has emerged for all flows is that the minimal seed is always spatially localized in all directions (Monokrousos et al., 2011; Rabin et al., 2012; Cherubini and De Palma, 2015; Pringle and Kerswell, 2010; Cherubini et al., 2015). The flow perturbation is characterized by an initial pattern that opposes the underlying mean shear di-

95 rection. Under the action of the Orr mechanism, the disturbance unpacks and gains in energy over a fast time scale as it rotates and aligns with the mean flow direction. This is followed by an oblique wave interaction mechanism that feeds energy into rolls. Then, the streamwise vortices generate streaks through the lift-up effect. For an initial amplitude just below E_c , the streak field is linearly

100 stable and the flow is attracted towards the laminar state. For an initial condition just above E_c , the streak field is unstable and breaks down to turbulence (Kerswell, 2018). The laminar/turbulent process for the minimal seed in pCF have been thoroughly investigated by (Monokrousos et al., 2011; Rabin et al., 2012; Duguet et al., 2013) where the preferential route to transition exhibits all

105 the different steps described above. Duguet et al. (2013) have also suggested a new scaling law for the minimal energy perturbation $E_c = O(Re^{-2.7})$, which is significantly smaller than previous estimates ($O(Re^{-2})$). In that same spirit, Cherubini et al. (2015) found a new scaling law for the kinetic energy threshold associated with asymptotic suction boundary layers ($E_c = O(Re^{-2})$). This

110 scaling differs from classical subcritical transition paths based on oblique waves (OW) or streamwise vortices (SV). What is notably fascinating is the fact that both the edge state and minimal seed exhibit well-known linear mechanisms (Orr, lift-up, secondary streak instability) that interact nonlinearly through the Navier-Stokes equations (Kerswell, 2018). This observation confirms the inter-

115 est for the development of a simplified set of equations that aims at modeling the dynamics close to the edge state.

A first attempt at simplifying the description of ECS in shear flows (pCf or plane channel flow) is given by Hall and Sherwin (2010); Blackburn et al. (2013) within the framework of the vortex/wave interaction (VWI) theory (Hall and Smith, 1991). In the limit of large Re , they reproduced the ECS found by Nagata (1990) by reduction of the Navier-Stokes equations to a two-dimensional problem for the streamwise-averaged velocity coupled to a linear inviscid eigenvalue problem for the instability wave where only a single streamwise Fourier mode is retained. The nonlinear feedback term is present in the streamwise-averaged part and maintains the amplitude of the streak. It further emphasized the predominant role of the critical layer of thickness $O(Re^{-1/3})$ by providing the appropriate interaction between the wave and the mean flow. In particular, Hall and Sherwin (2010) have shown that VWI theory is in perfect agreement with the numerical simulations of Wang et al. (2007). In that respect, the mechanism behind SSP can be seen as a finite-Reynolds number interpretation of the high- Re VWI theory. For a pCf, Deguchi et al. (2013); Deguchi (2015) made further theoretical progress to connect some asymptotical states given by VWI theory with localized ECS. The authors derived an energy scaling associated with a localized minimal state which closely matches the one found for the minimal seed ($O(Re^{-2.5})$ to compare with $O(Re^{-2.7})$). Beaume et al. (2014, 2015) extend the previous approach by retaining the leading-order diffusion terms in the streamwise perturbation equation. Interestingly, the formulation derived by Beaume et al. (2014, 2015) proved to be efficient at low Reynolds numbers and captures remarkably well the saddle-node bifurcation where the ECS separates into upper and lower branch states. Similar conclusions have recently been made by Pausch et al. (2019); Rosenberg and McKeon (2019) using analogous approximations for plane channel flow and pCf. In the same spirit, Alizard (2017); Alizard and Biau (2019) showed that this reduced system allows the computation of spanwise localized ECS and periodic orbits. Thomas et al. (2015); Farrell et al. (2017) have shown that this restricted nonlinear model (RNL) is also able to reproduce essential features of wall-bounded turbulent flows. In particular, Bretheim et al. (2015, 2018) showed that RNL models with

only a few number of selected streamwise Fourier modes (*i.e.* the band-limited RNL) are successful in predicting both mean flow and second-order statistics. Such reduction of wall-turbulence confirms the ability of RNL models to capture ECS embedded in the phase-space of the turbulent attractor.

Biau and Bottaro (2009) carried out nonlinear optimizations based on RNL equations to identify an optimal path to transition in a linearly stable duct flow. Using DNS, the authors proved that the resulting nonlinear optimal perturbation is able to reach self-sustained turbulence. By varying the value of the streamwise wavelength of the perturbation, they identified a cut-off around 300 wall units, below which no transition can be observed. The latter value is of the same order of magnitude as the minimal flow unit (Jiménez and Moin, 1991) for turbulence. Finally, the optimal solution exhibits strong similarities with the nonlinear solution lying on the edge. In the same way as in Biau and Bottaro (2009), Pralits et al. (2015) have found that nonlinear optimizations based on a RNL system with a single streamwise Fourier mode and two spanwise Fourier modes are successful in finding an optimal path according to the oblique wave scenario.

While previous studies have significantly enhanced our understanding of laminar/turbulent transition for subcritical flows, the minimal threshold energy obtained through nonlinear optimizations based on the RNL system has yet to be compared with the one corresponding to the minimal seed. How does the evolving flow structure of the corresponding nonlinear optimal perturbation compare with the one computed using RNL optimizations ? Furthermore, the generation of streamwise-independent vortices is a fundamental element in the laminar/turbulent transition process. However, it is not clear if the vortex generation mechanism is driven by the advection term (Hamilton et al., 1995) or the vortex stretching term (Schoppa and Hussain, 2002). Finally, most studies dealing with RNL models focused either on initial steps of transition (Biau and Bottaro, 2009) or on fully turbulent flow (Farrell and Ioannou, 2012). Can RNL models provide the whole picture of laminar/turbulent transition ? The scope of this paper is to shed some light on these major points. For that purpose, the

pCf case studied by Monokrousos et al. (2011); Duguet et al. (2013) is investi-
 180 gated. A single Fourier mode for the fluctuation will be retained hereafter that
 prevents any streamwise localization.

The paper is organized as follows. In section 2, we recall the equations of
 the RNL model. After presenting the Lagrangian functional to be maximized
 and numerical methods in section 3, we compare the kinetic energy thresholds
 185 found using RNL optimizations with those of the literature (Monokrousos et al.,
 2011; Duguet et al., 2013) and analyze the different steps of laminar/turbulent
 transition in section 4. A specific attention will be devoted to give physical
 insight into the initial streamwise vortex formation mechanism. Finally, section
 5 is dedicated to conclusions and perspectives.

190 2. Restricted non-linear system

We denote by x , y and z the coordinates in the streamwise, wall-normal
 and spanwise directions, respectively. We consider the plane Couette flow of
 an incompressible fluid with kinematic viscosity ν between two parallel plates
 located at $y = \pm h$. The two plates move in opposite directions with velocity
 $(\pm U_0, 0, 0)$. The Reynolds number is defined as $Re = U_0 h / \nu$. The over-bar will
 be used to distinguish quantities which are averaged over a streamwise distance
 L_x :

$$\bar{\phi}(y, z, t) = \frac{1}{L_x} \int_0^{L_x} \phi(x, y, z, t) dx. \quad (1)$$

The velocity perturbation to the Couette laminar solution ($U_b = y, 0, 0$) is
 decomposed into its streamwise-averaged part $\mathbf{U} = \bar{\mathbf{u}}$ and its fluctuation $\tilde{\mathbf{u}}$:

$$\mathbf{u}(x, y, z, t) = \mathbf{U}(y, z, t) + \tilde{\mathbf{u}}(x, y, z, t). \quad (2)$$

The components $\mathbf{u} = (u, v, w)$ will be called streamwise, wall-normal and span-
 wise velocities, respectively. For simplicity, \mathbf{U} will be referred to as the mean
 flow and (U, V, W) the components of the mean flow distortion: U correspond-
 ing to the streak and V, W to the roll components. The pressure is similarly

split into: $p(x, y, z, t) = P(y, z, t) + \tilde{p}(x, y, z, t)$. Using the scales h and U_0 , variables and equations will be expressed hereafter in non-dimensional form. We will consider a minimal RNL system where only a single streamwise component is retained. The fluctuation is thus expressed as: $\tilde{\mathbf{u}} = \hat{\mathbf{u}}e^{i\alpha x} + \hat{\mathbf{u}}^*e^{-i\alpha x}$, where $\alpha = 2\pi/L_x$ is the streamwise wave number. Under this hypothesis, only the components having streamwise wave numbers equal to $\pm 2\alpha$ contribute to the nonlinear terms in the equation $\tilde{\mathbf{u}} \cdot \nabla \tilde{\mathbf{u}} - \overline{\tilde{\mathbf{u}} \cdot \nabla \tilde{\mathbf{u}}}$. These terms are neglected in the present RNL model which can thus be viewed as a Galerkin truncation of the Navier-Stokes equations restricted to one streamwise Fourier mode. The system of equations governing the streamwise-averaged flow reads:

$$\begin{aligned}
V_y + W_z &= 0, \\
U_t + V(U + U_b)_y + WU_z &= D_v(U) - \partial_y(\hat{v}^*\hat{u} + \hat{v}\hat{u}^*) - \partial_z(\hat{w}^*\hat{u} + \hat{w}\hat{u}^*), \\
V_t + VV_y + WW_z &= -P_y + D_v(V) - \boxed{\partial_y(2\hat{v}\hat{v}^*) - \partial_z(\hat{w}^*\hat{v} + \hat{w}\hat{v}^*)}, \\
W_t + VW_y + WW_z &= -P_z + D_v(W) - \boxed{\partial_y(\hat{v}^*\hat{w} + \hat{v}\hat{w}^*) - \partial_z(2\hat{w}^*\hat{w})},
\end{aligned}$$

where $D_v = Re^{-1}(\partial^2/\partial y^2 + \partial^2/\partial z^2)$,

(3)

associated with homogeneous boundary conditions $U = V = W = 0$ on the walls. The Navier-Stokes equations, linearized around the mean flow, are:

$$\begin{aligned}
i\alpha\hat{u} + \hat{v}_y + \hat{w}_z &= 0, \\
\hat{u}_t + i\alpha(U + U_b)\hat{u} + \hat{v}(U + U_b)_y + V\hat{u}_y + \hat{w}U_z + W\hat{u}_z &= -i\alpha\hat{p} + d_v(\hat{u}), \\
\hat{v}_t + i\alpha(U + U_b)\hat{v} + \boxed{\hat{v}V_y} + V\hat{v}_y + \boxed{\hat{w}W_z} + W\hat{v}_z &= -\hat{p}_y + d_v(\hat{v}), \\
\hat{w}_t + i\alpha(U + U_b)\hat{w} + \boxed{\hat{v}W_y} + V\hat{w}_y + \boxed{\hat{w}W_z} + W\hat{w}_z &= -\hat{p}_z + d_v(\hat{w}),
\end{aligned}$$

where $d_v = Re^{-1}(-\alpha^2 + \partial^2/\partial y^2 + \partial^2/\partial z^2)$,

(4)

together with $\hat{u} = \hat{v} = \hat{w} = 0$ on the walls. Biau and Bottaro (2009) used a simplified version of the system (3,4) obtained by considering the following scaling: streaks are $O(1)$, rolls and the fundamental mode of the instability wave are $O(Re^{-1})$ and its harmonics are $o(Re^{-1})$. However, while the previous scaling is verified for the lower branch solution, it is not consistent when the whole process leading to turbulence is of interest. Indeed, the terms boxed

195

in equations (3) have to be balanced in equations (4) to guarantee total energy conservation. For that, the terms boxed in (4) have to be added. As a consequence, the roll can no longer be negligible in front of streak component and must also be considered. For the sake of conciseness, (3) will be denoted by $(\mathcal{F}(\mathbf{U}, P), \nabla \cdot \mathbf{U}) = \mathbf{0}$ and (4) as $(\mathcal{H}(\tilde{\mathbf{u}}, \tilde{p}), \nabla \cdot \tilde{\mathbf{u}}) = \mathbf{0}$.

3. Optimization based on the RNL system and numerical methods

In the present context, the nonlinear optimization consists in finding the initial perturbation that, for a fixed level of initial kinetic energy, has the largest growth for a given target time. First, we introduce the scalar product:

$$\left\langle \mathbf{u}, \mathbf{v} \right\rangle = \frac{1}{D} \int_{\mathcal{D}} \mathbf{u} \cdot \mathbf{v} \, dD \quad (5)$$

where \mathcal{D} is a rectangular parallelepiped bounded by the two plates and having L_x and L_z as streamwise and spanwise side lengths. The volume of \mathcal{D} is $D = 2 L_x L_z$ and $dD = dx \, dy \, dz$.

The function to maximize is the total kinetic energy for the perturbation which is divided in two parts:

$$E_{tot}(T) = E(T) + e(T) = \frac{1}{2} \left\langle \mathbf{U}(T), \mathbf{U}(T) \right\rangle + \frac{1}{2} \left\langle \tilde{\mathbf{u}}(T), \tilde{\mathbf{u}}(T) \right\rangle. \quad (6)$$

associated with the mean flow distortion and the fluctuating part (a sinusoidal function along x), respectively. The initial time is $t = 0$ and the target time at which the energy growth is maximized is noted $t = T$. Following Biau and Bottaro (2009); Olvera and Kerswell (2017), we search for the maximum of the constrained Lagrangian \mathcal{L} defined as

$$\mathcal{L} = E_{tot}(T) + \lambda \left(\left\langle \mathbf{U}_0, \mathbf{U}_0 \right\rangle - 2E_0 \right) + \zeta \left(\left\langle \tilde{\mathbf{u}}_0, \tilde{\mathbf{u}}_0 \right\rangle - 2e_0 \right) + \quad (7)$$

$$[\mathbf{A}, \mathcal{F}(\mathbf{U}, P)] + [\mathbf{a}, \mathcal{H}(\tilde{\mathbf{u}}, \tilde{p})] + [\Pi, \nabla \cdot \mathbf{U}] + [\pi, \nabla \cdot \tilde{\mathbf{u}}],$$

with $\mathbf{U}_0 = \mathbf{U}(t = 0)$, $\tilde{\mathbf{u}}_0 = \tilde{\mathbf{u}}(t = 0)$ and

$$[\mathbf{u}, \mathbf{v}] = \frac{1}{T} \int_0^T \left\langle \mathbf{u}, \mathbf{v} \right\rangle dt.$$

In the Lagrangian, $\mathbf{a} = (a, b, c)$, $\mathbf{A} = (A, B, C)$, π , Π and λ , ζ are the Lagrange multipliers. To determine the optimal initial perturbation, we write the first variations of \mathcal{L} with respect to the Lagrange multipliers, physical states (\mathbf{u} , \mathbf{U}) and the initial perturbations ($\tilde{\mathbf{u}}_0$, $\tilde{\mathbf{U}}_0$) and set them to zero. We recover equations (3), (4) and their adjoint counterparts. Adjoint equations and temporal initial and end conditions that close the system of equations are detailed in the appendix A. The strategy to converge to the solution corresponding to the maximum energy growth is based on successive time integration of direct and adjoint systems (similar to the power iteration method used in the linear framework) starting with an initial guess for the initial perturbation. Finally, at each step, both λ and ζ are chosen to ensure that $E(0) = E_0$ and $e(0) = e_0$ are satisfied. In the following, only the case $E_0 = 0$ is considered. Hereafter, the nonlinear optimal provided by the RNL model will be called either restricted nonlinear optimal or RNLOPT. One may remark that the function to maximize used by Biau and Bottaro (2009) and Pralits et al. (2015) is $e(t)$, the kinetic energy associated with the fluctuation. Nevertheless, for long times and close the threshold, the total kinetic energy is mainly driven by its mean flow contribution (see for instance (Duguet et al., 2013)). The restriction to $e(t)$ for the optimal gain is therefore not fully relevant for large target times.

For numerical integration of the RNL system (either direct or adjoint equations), spectral approximations of the velocity field are adopted, using Fourier expansions in both streamwise and spanwise directions and Chebyshev polynomials in wall-normal direction. The numerical methods are described in Alizard (2015) and the code has been validated in Alizard (2017). For the full Navier-Stokes equations, the spectral code developed by Buffat et al. (2011) is used. Finally, dealiasing with the 2/3 rule is implemented in the streamwise and spanwise directions for DNS and only in the spanwise direction for RNL simulations.

In the following, the flow cases investigated by Monokrousos et al. (2011); Duguet et al. (2013) are considered. The flow is simulated inside a computational box $(L_x, L_y, L_z) = (4\pi, 2, 2\pi)$ with periodic boundary conditions in x and z . Four Reynolds numbers are investigated $Re = 750, 1500, 2000$ and 3000 .

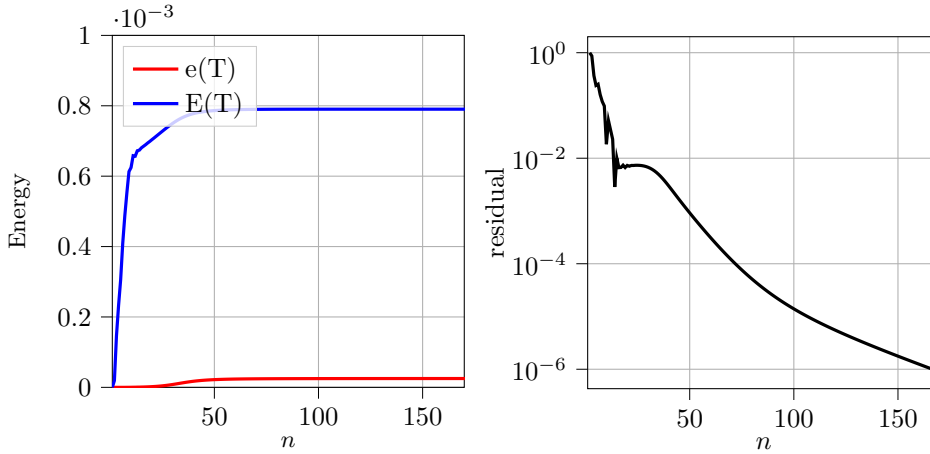


Figure 1: Convergence history for RNL optimizations for $Re = 3000$, $T = 140$ and $e_0 = 9 \times 10^{-8}$. Left: kinetic energy gains $e(T)$ and $E(T)$. Right: residual r .

Before dealiasing, accurate resolutions are used with $(N_y, N_z) = (81, 64)$ for $Re = 750$, $(N_y, N_z) = (81, 96)$ for $Re = 1500$ and $(N_y, N_z) = (101, 128)$ for $Re = 2000$ and 3000 for RNL simulations. For the DNS, the number of Fourier
240 modes in the streamwise direction is fixed to $N_x = 192$.

4. Results

4.1. Nonlinear optimizations and minimal threshold energy

First, an example of the convergence history is provided in figure 1 for $Re = 3000$, $T = 140$ and $e_0 = 9 \times 10^{-8}$. e_0 is chosen close to the kinetic
245 energy threshold. We introduce the residual $r = (E_{tot}^n - E_{tot}^{n-1}) / E_{tot}^n$ where the superscript n denotes the n^{th} iterate. A similar residual parameter is used by Cherubini and De Palma (2013). The figure shows that both $e(T)$ and $E(T)$ increase rapidly and reach a plateau in 60 iterations. For this target time, the kinetic energy is dominated by its streamwise averaged part. Then, a slow and
250 smooth decrease is observed for r . For the present study, the stopping criterion has been fixed to $r = 5 \times 10^{-6}$. For $R = 3000$, figure 2 shows the distributions of $e(t)$ and $E(t)$ for the same e_0 and various target times T . For $T < 80$, the total

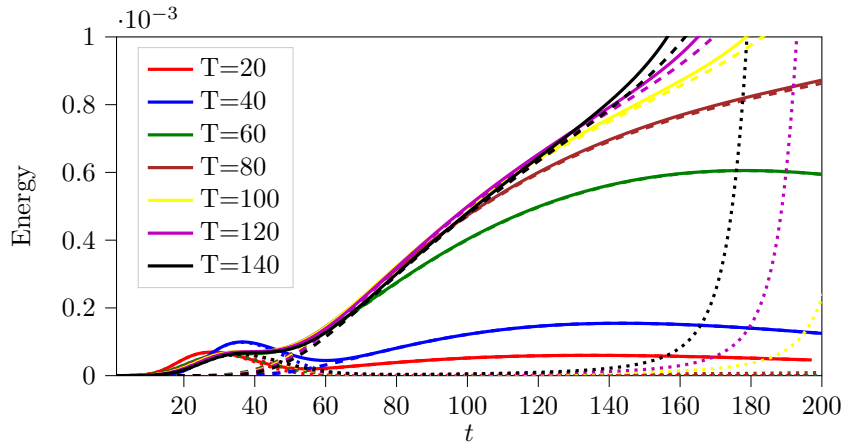


Figure 2: RNL optimizations: $Re = 3000$ and $e_0 = 9 \times 10^{-8}$. Time evolution of the total kinetic energy $E(t) + e(t)$ (full line), mean flow kinetic energy $E(t)$ (dashed lines) and fluctuation kinetic energy $e(t)$ (dotted lines) for various target times T .

kinetic energy is seen to grow before decaying. No breakdown is observed. When the target time is increased up to 80, both $E(t)$ and $e(t)$ are seen to increase for long times. This behavior is clearly observed for $T > 100$ in figure 2. {For $T < 40$, the total kinetic energy $E_{tot}(T)$ is mainly driven by $e(T)$. For larger target times T , the dominant contribution of $E_{tot}(T)$ is associated with $E(T)$. It is consistent with the results reported in figure 1(a) for $T = 140$. This a posteriori observation justifies the use of both contributions in the optimization process. For larger e_0 , $e(T)$ and $E(T)$ can reach equivalent gains. Nevertheless, being interested in the critical energy threshold, this case is not reported here. When the breakdown exists, $e(t)$ exhibits an exponential behavior for $t > T$. This is an indication that the state obtained at $t = T$ is linearly unstable and is driven along its unstable direction toward a chaotic saddle. Finally, the figure also suggests that, as T increases, the amount of initial kinetic energy e_0 necessary for the streak breakdown is slightly decreasing. {This behaviour is further illustrated in figure 3. For target times varying from $T = 30$ to 140, a bisection method together with the optimization algorithm is used to find the critical energy threshold e_c by listing whether or not a breakdown is observed

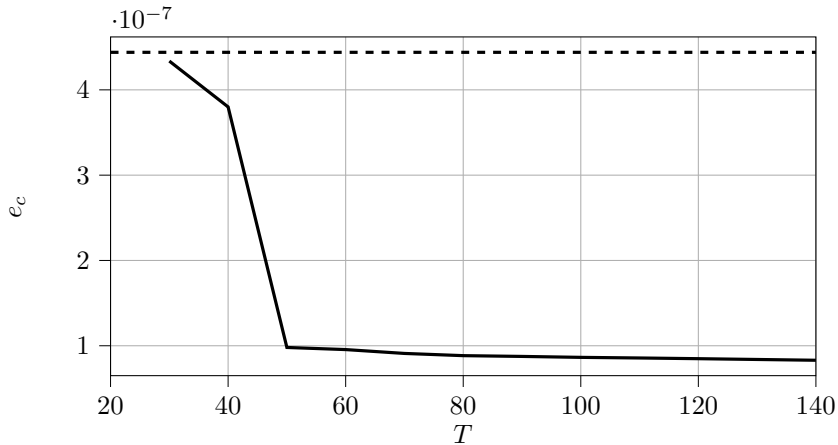


Figure 3: RNL optimizations: $Re = 3000$. Full line: critical initial energy threshold versus target time T . In dashed lines, the critical energy threshold for the oblique wave scenario is represented.

for long times. For e_0 just below e_c , the flow relaminarizes as t increases. For e_0 just above e_c , the perturbation breaks down to turbulence (within the RNL approximation) for large t . Figure 3 shows that for $T < 40$, e_c is close to the value given by Duguet et al. (2013) for the OW scenario. When $T > 50$, an abrupt change takes place with a strong decrease in e_c . Then, e_c exhibits a slow decay.

In figure 4, the kinetic energy of the perturbation is shown in the cross plane (y, z) at $t = 0$. It is seen that for $T = 40$, the perturbation is spatially extended in the spanwise direction and is symmetric with respect to the mid-plane $y = 0$. We recall that for this time, the critical energy threshold is close the one reported in the OW scenario (see figure 3). When increasing T , the optimal perturbation at the initial time becomes spanwise localized. This behavior is accompanied by a strong decrease in critical energy threshold e_c (figure 3). For T greater than 100, the mirror symmetry is broken. We observe a shift of the perturbation towards the lower wall associated with a slight decrease in e_c (figure 3) It is consistent with findings of Cherubini and De Palma (2014) who observed successive broken symmetries with an increase in target time within a

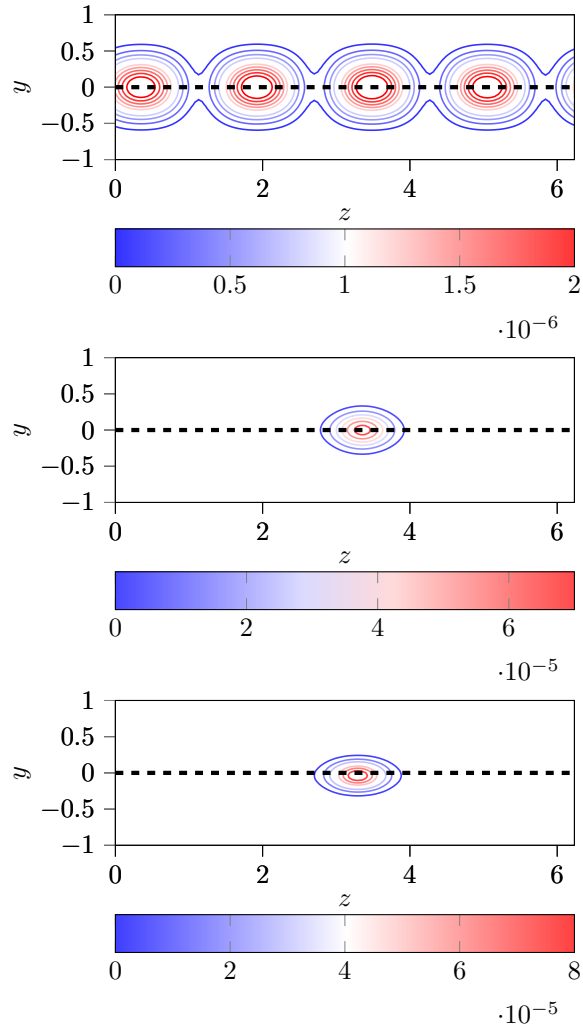


Figure 4: RNL optimizations: $Re = 3000$ and $e_0 = 9 \times 10^{-8}$. Kinetic energy of the fluctuation at $t = 0$ for $T = 40$, $T = 80$ and $T = 120$ (from top to bottom).

fully nonlinear optimization framework. Localized solutions in the wall-normal direction have also been observed in plane channel flow by Farano et al. (2016).

We now investigate the Reynolds number scaling for e_c . For that purpose, we have fixed $T = 110$ for both cases. For $Re = 3000$, we observe only a slight decrease in e_c when $T > 110$ (figure 3). This restricted minimal threshold e_c is shown in figure 5 for the same values of Reynolds numbers as those investigated by Duguet et al. (2009). Kinetic energy thresholds are also calculated by DNS. For that purpose, restricted nonlinear optimals are integrated forward in time using DNS for various values of the initial kinetic energy. Figure 5 shows that RNL simplification provides a good approximation of the threshold. It is also interesting to notice that we observe a power-law scaling $e_c = O(Re^\gamma)$ with $\gamma \approx -2.65$. The exponent is close to the one found using the full set of equations $\gamma = -2.7$ (Duguet et al., 2013). Especially, the restricted minimal perturbations found here have lower energy thresholds than those found for OW scenario. These results are also consistent with the theoretical analysis carried out by Deguchi (2015) ($\gamma = -2.5$). Part of this difference may be explained by the fact that Deguchi (2015) used an asymptotic theory designed for large Reynolds numbers.

4.2. Different paths associated with short and long target times.

We choose here to focus on the temporal evolution of RNLOPT for $Re = 2000$. Two target times are investigated $T = 50$ and $T = 110$. For $T = 50$, the initial energy is fixed to $e_0 \approx 2.64 \times 10^{-7}$; for $T = 110$, $e_0 \approx 2.54 \times 10^{-7}$. For both target times, e_0 is fixed close to the threshold e_c . For $T = 50$, the initial perturbation is symmetric with respect to $y = 0$. For $T = 110$, the mirror symmetry is broken, and the perturbation shows asymmetry with respect to the mid-plane $y = 0$ (similar to what is found for $Re = 3000$ as shown in figure 4). The restricted nonlinear optimal for $T = 50$ is referenced hereafter as RNLOPT_S. The one obtained for $T = 110$ will be denoted by RNLOPT_{NS}. The time integration is carried out using the RNL system (3, 4). Time evolutions of $e(t)$, $E(t)$ and E_{tot} are illustrated in figure 6. For both optimals, the breakdown

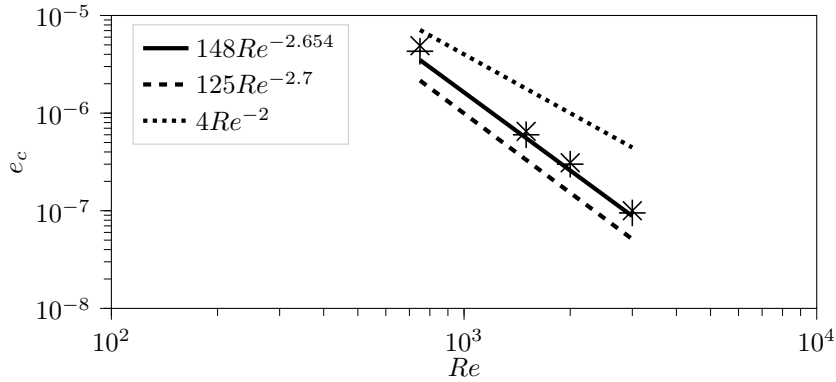


Figure 5: Energy threshold versus the Reynolds number Re for $Re = 750, 1500, 2000$ and 3000 found using RNL optimizations (full line). Symbols represent tested values of e_0 below/above which transition to turbulence never occurs when restricted nonlinear optimals are integrated forward in time using DNS. The fit $148Re^{-2.654}$ is compared to the fit $4Re^{-2}$ obtained for the oblique wave scenario for the same computational box and to the fit $125Re^{-2.7}$ associated with fully nonlinear optimizations (values given by Duguet et al. (2013)).

is observed for long times.

For $\text{RNLOPT}_{\mathbf{S}}$ and $\text{RNLOPT}_{\mathbf{NS}}$, the kinetic energy thresholds are also computed using DNS. The two RNLOPT are rescaled by bisection until an equilibrium is approached. The two threshold energy levels are not very different: $e_0 \approx 3.0 \times 10^{-7}$ and $e_0 \approx 3.12 \times 10^{-7}$, values to be compared with $e_0 \approx 2.54 \times 10^{-7}$ and $e_0 \approx 2.64 \times 10^{-7}$, respectively. For the minimal seed obtained using a fully non-linear approach, we recall that Duguet et al. (2013) found an energy threshold $\approx 1.53 \times 10^{-7}$. This level is thus about half the value provided by the restricted non-linear system. Figure 6 also compares $e(t)$, $E(t)$ and $E_{tot}(t)$ obtained either by the RNL system or the full Navier-Stokes equations. The two pairs of curves keep in close correspondence quite a long time, with a slight shift in amplitude for the DNS. In particular, $\text{RNLOPT}_{\mathbf{S}}$ and $\text{RNLOPT}_{\mathbf{NS}}$ exhibit different behaviors. While for the non-symmetric perturbation, a continuous increase in $E(t)$ is observed with an overshoot around $t = 600$, the symmetric perturbation shows a slight decrease in mean flow kinetic

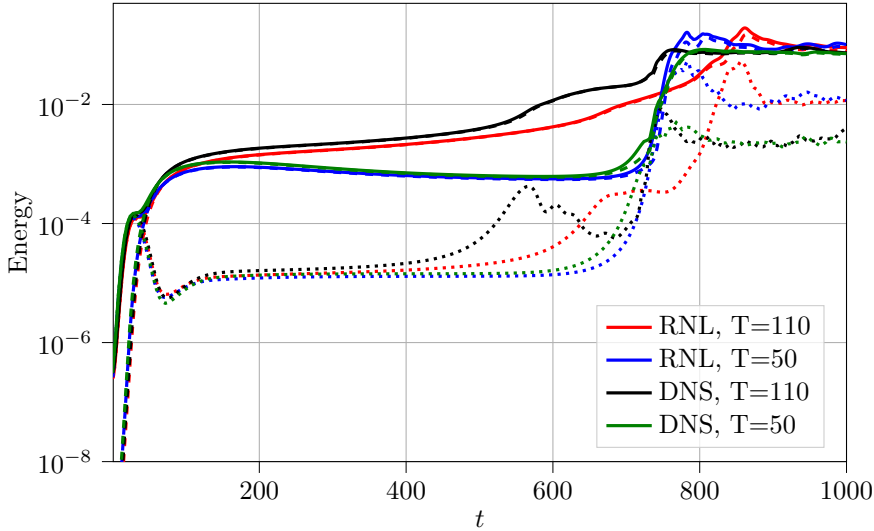


Figure 6: RNL simulations: $e_0 \approx 2.54 \times 10^{-7}$ and $e_0 \approx 2.64 \times 10^{-7}$ (for $T = 110$ and $T = 50$, respectively). The time evolution of $e(t)$ (dashed lines), $E(t)$ (dotted lines) and $E_{tot}(t)$ (full line) are shown. Results provided by DNS are also represented.

energy until it reaches a plateau near $t = 600$. These behaviors are found either using DNS or RNL simulation. It suggests that $\text{RNLOPT}_{\mathbf{S}}$ and $\text{RNLOPT}_{\mathbf{NS}}$ pass along different edge states before the breakdown.

335 In figure 7, we compare transverse cross-sections for the spanwise vorticity component for the two optimals at the earliest times. While the first optimal exhibits symmetry with respect to the mid-plane $y = 0$, the other one is shifted to the lower side. The time evolution of the two flows is very similar. At the initial time, the fluctuation is characterized by a flow pattern that opposes the
 340 mean shear direction. As time evolves from $t = 0$ to $t = 20$, the perturbation tilts downstream thus causing transient growth of energy. At $t = 20$, an increase in kinetic energy of the streamwise velocity component is also observed (not shown here). This suggests that a combination of Orr and lift-up mechanisms leads to enhance energy gain for these times (Butler and Farrell, 1992).

345 For $t = 30$, the figures 8(a,b) show that the streamwise-averaged part has a simple form that involves spanwise localized streamwise rolls and low- and high-

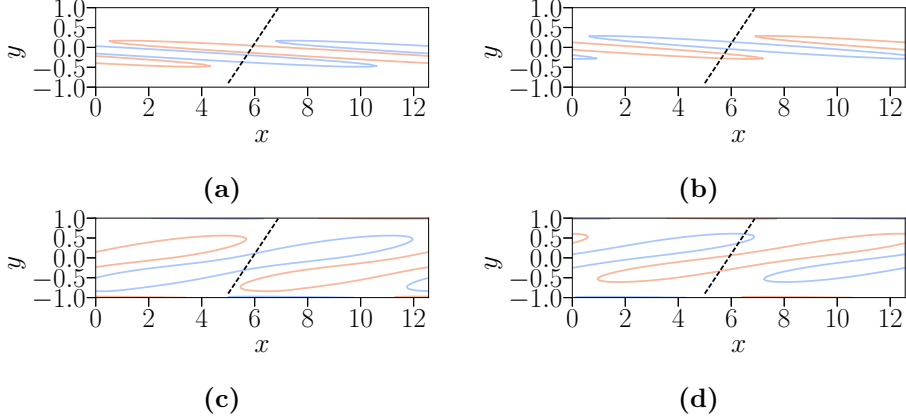


Figure 7: RNL simulation. RNLOPT_{NS} (a,c) and RNLOPT_S (b,d) for $e_0 = 2.54 \times 10^{-7}$ ($T = 50$) and $e_0 = 2.64 \times 10^{-6}$ ($T = 110$). Spanwise vorticity fluctuation at $t = 0$ (a,b) and $t = 20$ (c,d) in the (x, y) plane at $z = L_z/4$. For $t = 0$ levels ± 20 , for $t = 20$ levels ± 100 . The profiles of the streamwise-averaged velocity are also shown in black dashed lines.

speed streaks on both walls. However, for RNLOPT_{NS}, the symmetry breaking has enhanced the development of the high-speed streak in the upper-half of the domain (panel (b)). For $t = 400$, this high-speed streak has moved towards the lower ($y = -1$) wall. For this time, the mean flow associated with RNLOPT_{NS} is mainly driven by a single high-speed streak sandwiched between two low-speed streaks (figure 8(d)). On the contrary, RNLOPT_S is characterized by a mirror symmetry about the plane $y = 0$. Especially, the figures 8(a,c) show that the streaks are centered with a similar distance from both walls for $t = 30$ and $t = 400$. We recall that at the initial time $E_0 = 0$, meaning that the streamwise averaged part is null at $t = 0$. The only source for generating rolls (V, W) is due to the nonlinear feedback term that represents the quadratic interaction of the fluctuating part. Rolls then redistribute the streamwise component of momentum and create streaks (U). RNLOPT_S and RNLOPT_{NS} exhibit then two fundamentals elements of the SSP (Hamilton et al., 1995; Waleffe and Kim, 1997).

In figure 9, we show a reconstruction of three-dimensional flow fields at $t = 700$. For this specific time, an almost equilibrium is observed for both opti-

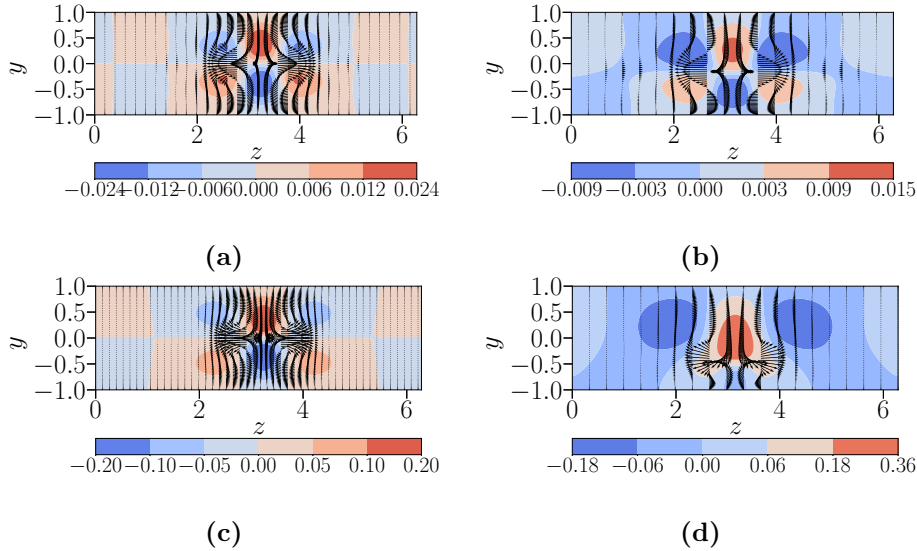


Figure 8: RNL simulation. RNLOPT_S (a,c) and RNLOPT_{NS} (b,d) for $e_0 = 2.64 \times 10^{-7}$ ($T = 50$) and $e_0 = 2.54 \times 10^{-7}$ ($T = 110$), respectively. Isolevels of the streamwise component of the mean flow distortion U and vectors for the cross-stream components at $t = 30$ (a,b) and $t = 400$ (c,d).

mals. For RNLOPT_S, the structure consists of undulated streaks on both walls.
 365 The solution associated with RNLOPT_{NS} exhibits an isolated bent high-speed
 streak sandwiched between two low-speed streaks. The observed motion for
 both optimals shares similarities with travelling wave solutions associated with
 lower branch states (Waleffe, 1998; Gibson and Brand, 2014). The time evolving
 flow structures associated with both RNLOPT_S and RNLOPT_{NS} obtained by
 370 DNS are shown in figure 10. Similar patterns are observed confirming, at least
 quantitatively, the good approximation provided by the RNL system. On one
 hand, the time-evolving structure for RNLOPT_{NS} bears a striking resemblance
 to the time evolution of the minimal perturbation identified by Monokrousos
 et al. (2011); Rabin et al. (2012); Duguet et al. (2013). On the other hand,
 375 the symmetric optimal exhibits a pattern similar to the lower branch spanwise-
 localized solutions found by Gibson and Brand (2014). For this perturbation,
 the state found by Monokrousos et al. (2011); Rabin et al. (2012); Duguet et al.

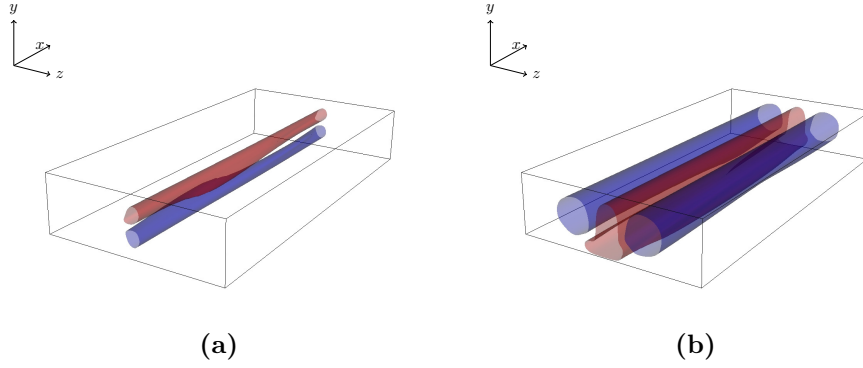


Figure 9: RNL simulation. RNLOPT_S (a) and RNLOPT_{NS} (b) for $e_0 \approx 2.64 \times 10^{-7}$ ($T = 50$) and $e_0 \approx 2.54 \times 10^{-7}$ ($T = 110$), respectively. Snapshots of the solution extracted at $t = 700$. The instantaneous streamwise velocity $u = U + \tilde{u}$ is considered. Isosurfaces ± 0.1 are shown in red and blue.

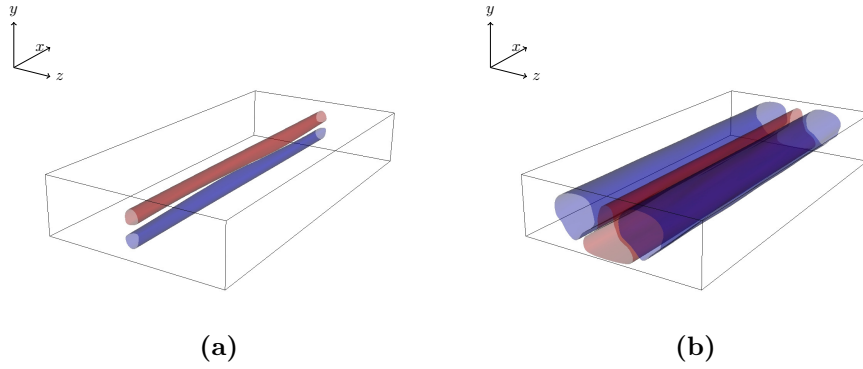


Figure 10: DNS results. (a) RNLOPT_S, $e_0 \approx 3.12 \times 10^{-7}$ and (b) RNLOPT_{NS}, $e_0 \approx 3 \times 10^{-7}$. Snapshots of the solution extracted at $t = 700$. Isosurfaces ± 0.1 are shown in red and blue.

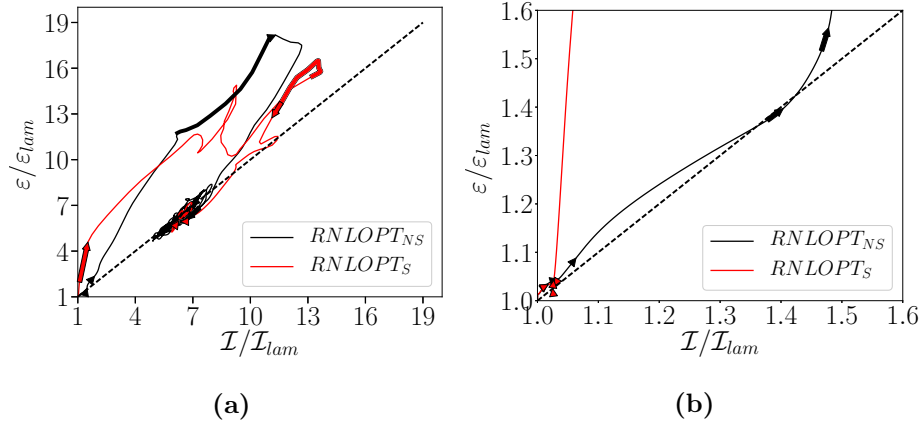


Figure 11: RNL simulation. Energy input/dissipation rate trajectories starting from $\text{RNLOPT}_{\mathbf{S}}$ and $\text{RNLOPT}_{\mathbf{NS}}$. Values are scaled by their laminar states $(\mathcal{I}_{lam}, \varepsilon_{lam})$. Time direction is indicated by arrows. Arrow length corresponds to a time interval $\Delta t = 10$. A zoom area of (a) is shown in (b). For both optimals bottom arrow positions are fixed at $t = 750, 800, 850, 900$ in panel (a) and at $t = 100, 300, 600$ and 700 in panel (b).

(2013) is never recovered because the streaks on the upper wall and on the lower wall develop secondary instability at the same time.

To further characterize the dynamics associated with the two optimals and their connection with results reported in the literature, the phase space trajectories are studied in the energy input / dissipation rate plane. The rate of change of energy equation is equal to $\mathcal{I} - \varepsilon$, where the energy input \mathcal{I} and dissipation rate ε read

$$\mathcal{I} = \frac{1}{Re} + \frac{1}{DRe} \int_0^{L_x} \int_0^{L_z} \left(\frac{\partial u}{\partial y} \Big|_{y=1} + \frac{\partial u}{\partial y} \Big|_{y=-1} \right) dx dz,$$

$$\text{and } \varepsilon = \frac{1}{Re} + \frac{1}{DRe} \int_{\mathcal{D}} \nabla \mathbf{u} : \nabla \mathbf{u} dD.$$

380 The trajectories for both optimals are shown in figure 11.

For $\text{RNLOPT}_{\mathbf{S}}$, the perturbation spends a long time close to $(\mathcal{I}/\mathcal{I}_{lam}, \varepsilon/\varepsilon_{lam}) \approx (1.03, 1.03)$ where the energy input is balanced by the dissipation rate. Especially, figure 11(b) shows that between $100 < t < 700$, the corresponding points in the phase space $(\mathcal{I}/\mathcal{I}_{lam}, \varepsilon/\varepsilon_{lam})$ are sitting in the neighborhood of

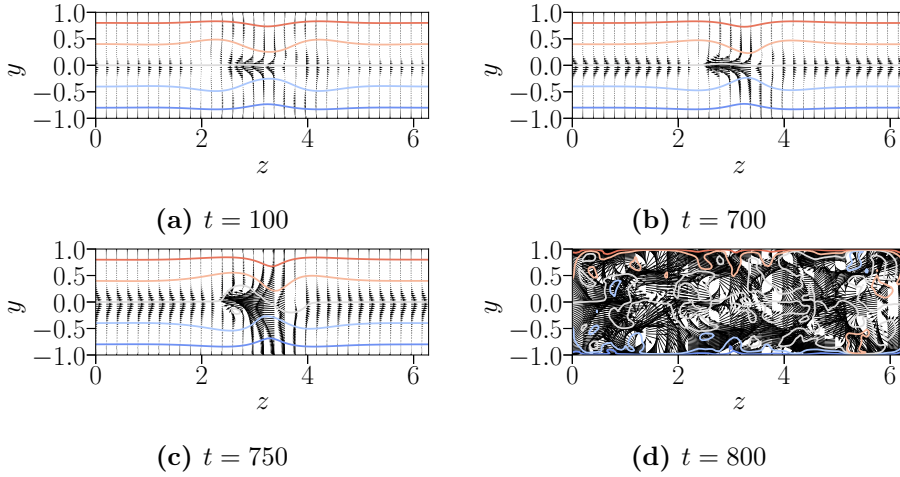


Figure 12: RNL simulation for RNLOPT_s. Cross-sections of the full velocity field in the plane $x = 6$, for times $t = 100, 700, 750$ and 800 . Contours: iso-levels of $U_b + u$ ($-0.8, -0.4, 0, 0.4, 0.8$); arrows: (v, w) vectors. The vectors are normalized by the square of the total kinetic energy for each time.

385 (1.03, 1.03). Cross-sections of the full velocity field $(u + U_b, v, w)$ in the plane $x = 6$ are shown in figure 12 for $t = 100, 700, 750$ and 800 . Some iso-contours of the streamwise velocity are reported along with the corresponding cross-flow vectors. The choice of $x = 6$ is arbitrary. The figure shows that the flow remains symmetric with respect to the horizontal axis $y = 0$ until $t \approx 700$. It
390 corresponds to a pair of low- and high-speed streaks on both walls that are almost steady (the vortex motion in the plane $x = 6$ have the same orientation for both $t = 100$ and 700). For $t = 750$, the mirror symmetry associated with the plane $y = 0$ is broken. In figure 13, cross-section of the velocity fields is shown in the plane $y = -0.5$ for $t = 750$. For this specific time, both streaks
395 exhibit a sinuous motion. For $750 < t < 800$, the flow follows a trajectory characterized by high values of the dissipation rate (≈ 16 see figure 11(a)). For these times, the flow breaks down to RNL turbulence and is rapidly spreading in the spanwise direction until the whole computational domain is filled by unsteady vortex motions (see figure 12(d)). For $t > 900$, the flow is attracted to
400 a chaotic saddle (figure 11(a)). This behaviour corresponds to a bursting

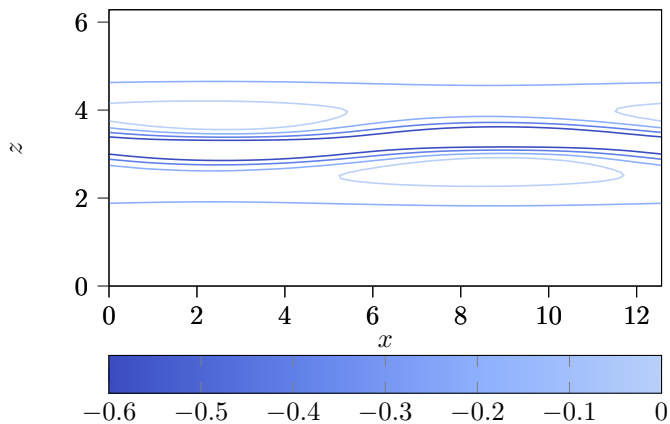


Figure 13: RNL simulation for RNLOPT_S. Cross-sections of the full velocity field in the plane $y = -0.5$, for time $t = 750$. Contours: iso-levels of $U_b + u$.

event characterized by highly dissipative perturbations as shown by Cherubini and De Palma (2013). However, Cherubini and De Palma (2013) have found that the highly dissipative nonlinear optimal disturbances pass closer to an edge-state and they are rapidly repelled away from it. For the symmetric RNL
405 optimal, the trajectory seems to spend a long time in the vicinity of an edge state. Nevertheless, before drawing hasty conclusions, such a state should be computed using Newton algorithm. For the second optimal mode (*i.e.* $T = 110$ corresponding to RNLOPT_{NS}), the flow structure passes close to the point $(\mathcal{I}/\mathcal{I}_{lam}, \varepsilon/\varepsilon_{lam}) \approx (1.03, 1.03)$ ($t \approx 100$) and is rapidly repelled away from it
410 (see time $t = 300$ in figure 11(b)). However, for $t \approx 700$, the trajectory exhibits a typical cusp-like behavior when approaching the point $(1.35, 1.35)$ on the diagonal (figure 11(b)). Near this state, the structure is shown in figure 9(b). Cross-sections of the full velocity field are shown in figure 14 at $x = 6$ for t varying from 100 to 850. The figure shows that for $t = 100$, the pattern is almost similar as the one associated with RNLOPT_S. For $t = 300$, the streak in
415 the upper-half of the domain has developed more rapidly than the one located on the other side. In addition, the flow, for $100 < t < 600$, is characterized by an unsteady vortex in the plane $x = 6$ which differs from the behavior ob-

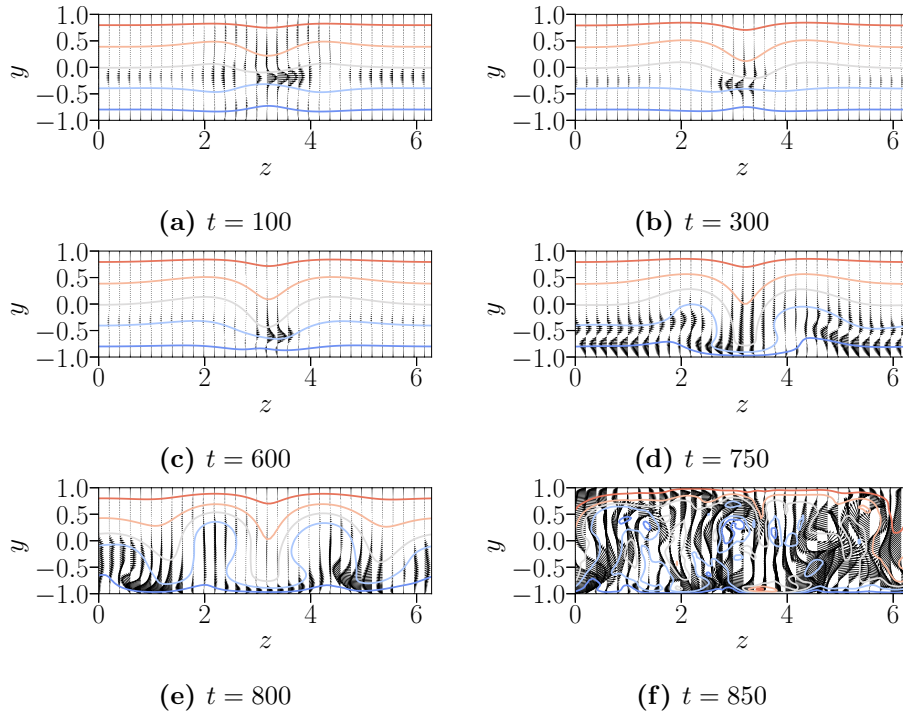


Figure 14: RNL simulation for RNLOPT_{NS}. Cross-sections of the full velocity field in the plane $x = 6$, for times $t = 100, 300, 600, 750, 800,$ and 850 . Contours: iso-levels of $U_b + u$ ($-0.8, -0.4, 0, 0.4, 0.8$); arrows: (v, w) vectors. The vectors are normalized by the square of the total kinetic energy for each time.

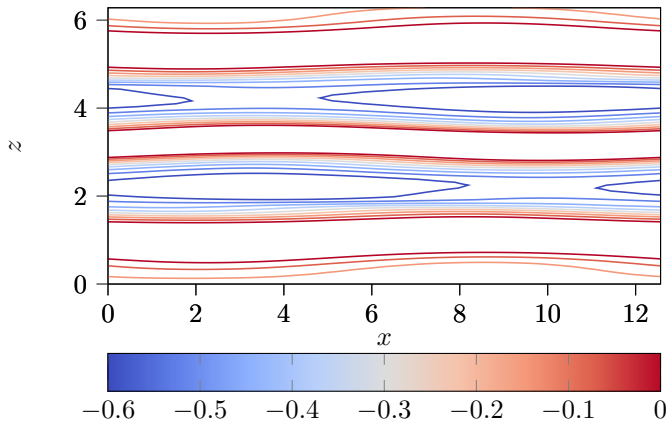


Figure 15: RNL simulation for RNLOPT_{NS}. Cross-sections of the full velocity field in the plane $y = 0$, for time $t = 800$. Contours: iso-levels of $U_b + u$.

served for RNLOPT_S. For $t = 750$, the two low-speed streaks have developed
420 on the sides of the high-speed streak. For $t = 800$, the pattern is mainly driven
by the low-speed streaks. In figure 15, cross-section of the full velocity fields:
 $(U_b + u, v, w)$ in the plane $y = 0$ is shown for $t = 800$. For this time, the low
speed streaks exhibit a varicose symmetry. For $800 < t < 810$, the trajectory is
seen to reach high values of dissipation and is rapidly attracted to the chaotic
425 saddle (figure 11(a)). In contrast with the symmetric perturbation, the flow
passes close to the edge state (for $700 < t < 750$), but it is rapidly repelled away
from it. Hence, the bursting event associated with the breakdown of the low
speed streaks appears to be closely related to the bursting scenario investigated
by Cherubini and De Palma (2013). For the non-symmetric perturbation, the
430 path leading to RNL turbulence closely resembles the one corresponding to the
minimal seed (Duguet et al., 2013) except that the optimal is not localized in
the streamwise direction at the earliest times. In particular, a striking resem-
blance of the patterns shown in figure 14 with those displayed in figure 8 in
Duguet et al. (2013) can be observed. In addition, the varicose symmetry is
435 also observed by the previous authors.

To further compare RNL simulations and DNS, the paths in the energy

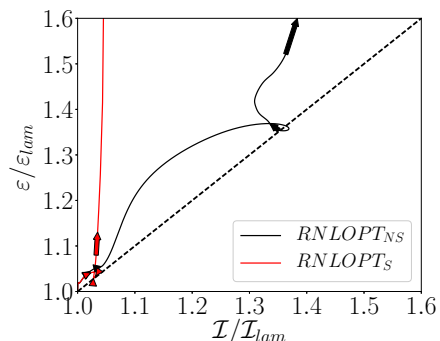


Figure 16: DNS. Energy input/dissipation rate trajectories starting from RNLOPT_S and RNLOPT_{NS}. Values are scaled by their laminar states $(\mathcal{I}_{lam}, \varepsilon_{lam})$. Time direction is indicated by arrows. Arrow length corresponds to a time interval $\Delta t = 10$. Bottom arrow positions are fixed at $t = 100, 300, 600$ and 700 .

input/dissipation rate plane provided by the DNS are also shown in figure 16. From a geometrical viewpoint, trajectories exhibit the same characteristics as the ones found using RNL system. Especially, the trajectory associated with RNLOPT_{NS} also exhibits an almost equilibrium point around $(\mathcal{I}/\mathcal{I}_{lam}, \varepsilon/\varepsilon_{lam}) \approx (1.35, 1.35)$. For RNLOPT_S, the path in the plane $(\mathcal{I}/\mathcal{I}_{lam}, \varepsilon/\varepsilon_{lam})$ is seen to approach the point $(1.03, 1.03)$ before being repelled.

The space-time diagram associated with the DNS and RNL simulations are displayed in figure 17 for RNLOPT_{NS} (the case RNLOPT_S is not shown here). The figure shows the time evolution of the spanwise distribution for the wall-shear stress on the lower wall, normalized with the laminar value. Figures 17(a) and (b) show that while the streak breakdown takes place in a narrow region at $t \approx 700$ along the spanwise direction, it spreads rapidly along z for larger times for both DNS and RNL simulations. We also observe that the spanwise spreading is similar whether the RNL system or the full Navier-Stokes equations are used. Nevertheless, some differences can be observed. The streak breakdown seems to start at different times ($t > 600$ for RNL and $t < 600$ for DNS). It is consistent with the results shown in figure 6 where the increase in $E(t)$ (the kinetic energy associated with the streamwise averaged part) starts near $t \approx 550$ for DNS and $t \approx 650$ for RNL. The friction at the wall appears also to reach

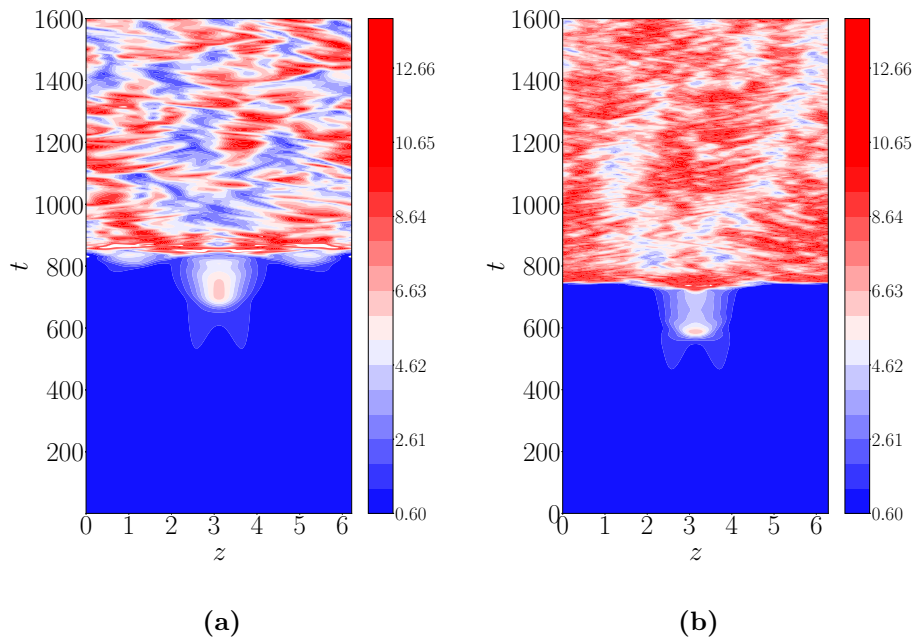


Figure 17: Spatiotemporal diagram obtained using (a) RNL simulation and (b) DNS for $\text{RNLOPT}_{\text{NS}}$ near the threshold. Isocontours of the wall shear stress based on the streamwise-averaged velocity field normalized with the laminar value.

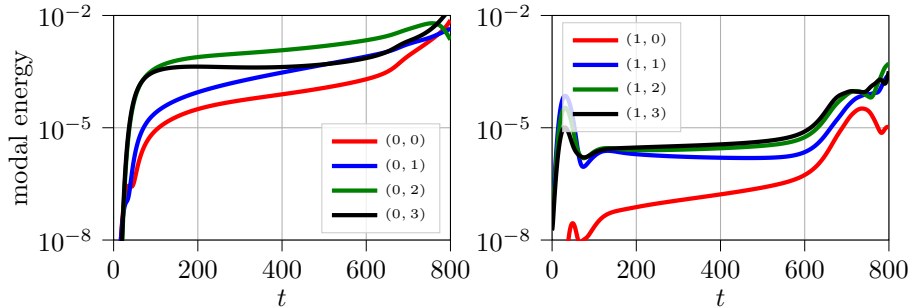


Figure 18: RNL simulation. Energy in selected Fourier components for RNLOPT_{NS} ($T = 110$) for the kinetic energy threshold $e_0 \approx 2.54 \times 10^{-7}$. Left: streamwise mean flow components, right: modes for the fundamental streamwise wavenumber.

higher values when using DNS.

4.3. Modal energy and origin of streamwise independent rolls and streaks

First, we analyze the spectral energy distribution of the Fourier modes for the time evolving flow structure associated with RNLOPT_{NS}. Aiming to discuss the physical mechanisms in the light of those associated with the minimal seed, only RNLOPT_{NS} is considered. Fourier modes corresponding to the wavevector components $(n\alpha, m\beta)$ with $(\alpha, \beta) = (2\pi/L_x, 2\pi/L_z)$ are hereafter labeled with couples (m, n) . The time evolution of the disturbance energy for 8 selected Fourier components can be seen in figure 18. The flow is symmetric in spanwise direction implying that the energy of the modes $(n, -m)$ are equal to their positive counterpart (n, m) .

At initial time, the most energetic modes are $(1, \pm 1)$, $(1, \pm 2)$ and $(1, \pm 3)$. Later, the oblique waves experience transient growth while generating streamwise rolls associated with the $(0, 2)$ and $(0, 3)$ components. For $t \approx 50$, most of the energy is transferred into $(0, 2)$ and $(0, 3)$. At about this time, streamwise rolls and streaks located on the upper and the lower walls are identified as the dominant flow pattern (see figure 8(b)). As time increases up to 600, the mode $(0, 1)$ reaches the same level as $(0, 3)$ and the perturbation maintains an almost constant trend. At this time, the flow dynamics is driven by a single

475 high-speed streak (see figure 14(c)). Due to the loss of symmetry with respect
 to the plane $y = 0$, the mean rolls located near the upper wall displace high-
 speed fluid towards the central region and amplify the high-speed streak (for
 $100 < t < 600$). Then, modes $(1, 2)$ and $(1, 3)$ grow significantly. For $t > 750$,
 the pair of low-speed streaks appears to contribute mainly to the flow dynamics
 480 (see figure 14(d,e)). It should then indicate that at $t = 600$, the high-speed
 streak fields is unstable. This has for consequence to amplify modes $(1, 2)$ and
 $(1, 3)$. Nonlinear interactions of these waves modify the streamwise rolls that,
 in turn, generate the pair of low-speed streaks. The dynamics exhibits then a
 strong interplay between the time varying meanflow and the superimposed per-
 485 turbation. For the minimal seed, the most energetic modes at $t = 0$ are of the
 type $(0, m)$ with also a significant contribution of $(1, \pm 1)$, $(2, \pm 1)$, $(3, \pm 1)$ and
 $(4, \pm 1)$ (Duguet et al., 2013). At the early stage, Duguet et al. (2013) indicate
 that modal interactions are driven by oblique waves. Then, most of the energy
 is transferred to $n = 0$ modes with a major contribution for $m = 2$, $m = 3$
 490 and $m = 4$. In particular, for these times, the kinetic energy associated with
 the fundamental $n = 1$ and its harmonics are less important. In the present
 work, we prevent any contribution of the streamwise-averaged component and
 its harmonics in α at $t = 0$. Hence, the initial perturbation obtained within the
 RNL approximation cannot reproduce the true nonlinear optimal. This may
 495 explain the differences observed in the critical energy thresholds. However, the
 dynamics for short times is also driven by oblique wave interactions that gener-
 ate $(0, 2)$ and $(0, 3)$. At this time, we also observe a minor contribution of the
 mode $n = 1$.

The streamwise vortices generation mechanisms are now addressed for RNLOPT_{NS}
 for $t < 50$. This time interval corresponds to the initial stages for rolls produc-
 tion. For these times ($t < 50$), we see no notable differences in modal kinetic
 energies for RNLOPT_S and RNLOPT_{NS} (see figure 6) and the mechanisms
 behind mean rolls production are quite identical (not shown here). The mech-
 anisms are examined on the basis of vorticity considerations. In the following,

we consider the equation for the mean streamwise vorticity:

$$\begin{aligned} \frac{\partial \Omega_x}{\partial t} + V \frac{\partial \Omega_x}{\partial y} + W \frac{\partial \Omega_x}{\partial z} = \frac{1}{Re} \left(\frac{\partial^2}{\partial y^2} + \frac{\partial^2}{\partial z^2} \right) \Omega_x + \Omega_y \frac{\partial U}{\partial y} + \Omega_z \frac{\partial U}{\partial z} + \\ \underbrace{\frac{\partial^2}{\partial y \partial z} (\overline{\tilde{v}^2} - \overline{\tilde{w}^2})}_{P_1} + \underbrace{\left(\frac{\partial^2}{\partial y^2} - \frac{\partial^2}{\partial z^2} \right) \overline{\tilde{v}\tilde{w}}}_{P_2}. \end{aligned} \quad (8)$$

This equation (8) was also studied by Gessner (1973) in order to explain the nature of the streamwise eddies observed in turbulent flows along corners. In equation (8), the term $\Omega_y \partial U / \partial y + \Omega_z \partial U / \partial z$ is null (we recall that the streamwise averaged flow is independent of x). As a result, the only source terms in (8) are P_1 and P_2 . Note that P_1 and P_2 have the same physical origin and it is simple to show that $P_1 + P_2$ can be reduced to the form P_1 after projection on the principal axes of the Reynolds tensor (restricted to the plane (y, z)) (Perkins, 1970).

In figure 19, we show the cross-sections of $\overline{\tilde{v}^2}$, $\overline{\tilde{w}^2}$ and $\overline{\tilde{v}\tilde{w}}$ at $t = 30$. The component $\overline{\tilde{w}^2}$ has a maximum value $\approx 6 \times 10^{-4}$. The contour peaks are $\approx 2 \times 10^{-5}$ and $\approx 4 \times 10^{-6}$ for $\overline{\tilde{v}\tilde{w}}$ and $\overline{\tilde{v}^2}$, respectively. Hence, the component $\overline{\tilde{w}^2}$ appears as the most important contribution, thereby reflecting the sinuous character of the perturbation at $t = 30$. For this time, it can be noted that the critical layer is almost horizontal near $y = 0$. According to the VWI theory, the wave's Reynolds stress is mainly amplified within the critical layer through the action of \tilde{w} in agreement with our observations (Hall and Sherwin, 2010). Figure 20 shows the cross-derivative of $\overline{\tilde{w}^2}$ along y and z : $-\partial^2 \overline{\tilde{w}^2} / \partial y \partial z$ together with $P_1 + P_2$. The figure shows a close correspondence between both contours indicating that $-\partial^2 \overline{\tilde{w}^2} / \partial y \partial z$ mainly contributes to $P_1 + P_2$. Thus, we can observe that the nonlinear self-interaction of the streamwise-varying mode produces mean streamwise vorticity in exactly the right place where streamwise rolls are identified in figure 8.

Equation (8) is obtained by straightforward application of curl operator on the streamwise-averaged momentum equation (the term $P_1 + P_2$ is simply the curl of the Reynolds stress term). The role of Reynolds stress in generating

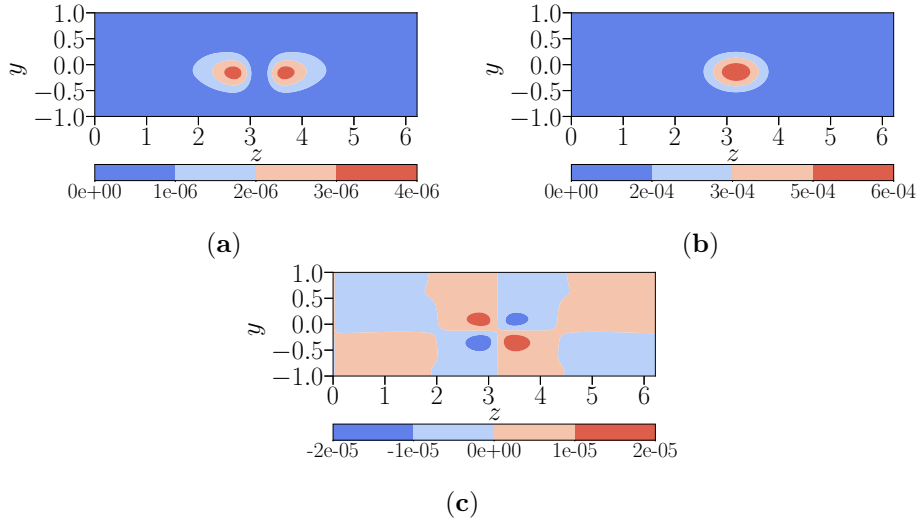


Figure 19: RNL simulation. Reynolds stress components for RNLOPT_{NS} ($T = 110$) and $e_0 \approx 2.54 \times 10^{-7}$ extracted at $t = 30$. $\overline{v\overline{v}}$ (a), $\overline{w\overline{w}}$ (b) and $\overline{v\overline{w}}$ (c).

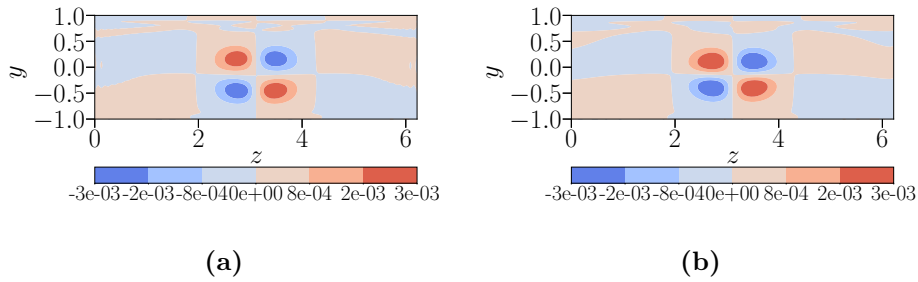


Figure 20: RNL simulation. RNLOPT_{NS} ($T = 110$) and $e_0 = 2.54 \times 10^{-7}$. Snapshots extracted at $t = 30$. Production term: $P_1 + P_2$ (a) and contribution $-\partial^2 \overline{w^2} / \partial y \partial z$ to $P_1 + P_2$ (b).

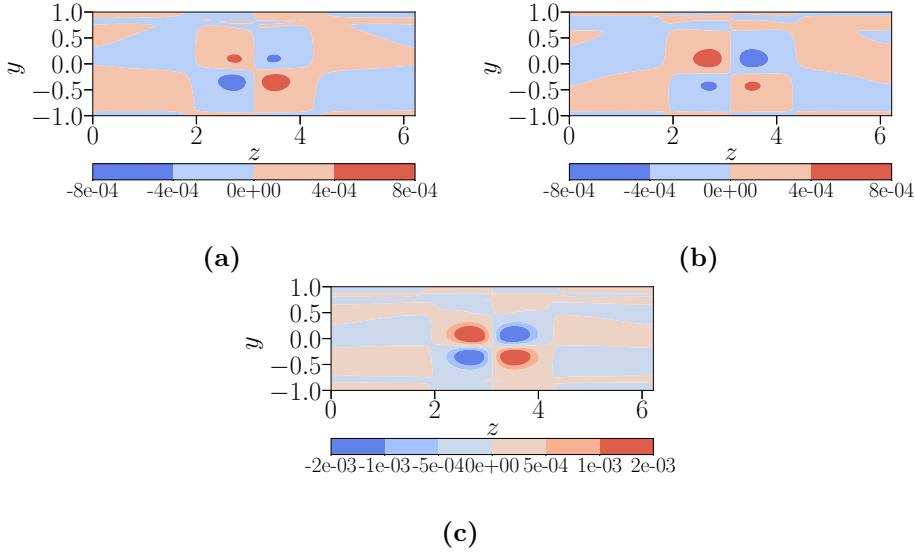


Figure 21: RNL simulation. RNLOPT_{NS} for $T = 110$ and $\epsilon_0 = 2.54 \times 10^{-7}$. Gain or loss of mean streamwise vorticity due to the fluctuating components. Snapshots extracted at $t = 30$. (a) stretching term P_s ; (b) tilting term P_t ; (c) convective term P_c .

mean vorticity can be grasped by thinking of it in terms of anisotropic pressure *i.e.* a pressure whose the mean value depends on orientation. An alternative for getting the transport equation of Ω_x is to start from the local vorticity equation and take the average of it in the streamwise direction. For a discussion of the obtained equation that offers a description in terms of vorticity dynamics, the reader may consult Tennekes and Lumley (1972). The method leads to an alternative expression of $P_1 + P_2$ involving correlations between fluctuating vorticity components $(\tilde{\omega}_x, \tilde{\omega}_y, \tilde{\omega}_z) = \nabla \times \tilde{\mathbf{u}}$ and the associated strain rates:

$$P_1 + P_2 = \underbrace{\overline{\tilde{\omega}_x \frac{\partial \tilde{u}}{\partial x}}}_{P_s} + \underbrace{\overline{\tilde{\omega}_y \frac{\partial \tilde{u}}{\partial y}} + \overline{\tilde{\omega}_z \frac{\partial \tilde{u}}{\partial z}}}_{P_t} - \underbrace{\overline{\frac{\partial \tilde{v} \tilde{\omega}_x}{\partial y}} - \overline{\frac{\partial \tilde{w} \tilde{\omega}_x}{\partial z}}}_{P_c} \quad (9)$$

In (9), P_s and P_t , the so-called vortex stretching and vortex tilting terms, respectively, represent amplification and rotation of the vorticity vector by the strain rate. The convective term P_c represents the mean transport of $\tilde{\omega}_x$ by the fluctuating velocity. Cross-sections of P_s , P_t and P_c are shown in figures 21 for $t = 30$. All terms are mainly localized in the area where mean streamwise

vortices are generated (see figure 8). Besides that, the figure 21 shows that levels associated with P_c are nearly three times higher than those of P_s and P_t . For this time, P_c contributes then mainly to rolls production. We recall that Hamilton et al. (1995) proposed a streamwise vortex generation mechanism, in
 530 which the advection term P_c plays the dominant role (see also for a review Kim (2011)). Then, the mechanism behind the streamwise vortices generation at the initial time appears closer to the one identified by Hamilton et al. (1995).

The term P_c is analogous to the Reynolds-stress term in the equation of the mean velocity. It appears with the opposite sign in the transport equation of the
 535 fluctuating vorticity and is hence responsible of an exchange of mean enstrophy between the component attached to the mean velocity and that related to the fluctuation. This term is mainly driven by the correlation $\overline{\tilde{v}\tilde{\omega}_x}$ (not shown here). In the context of fully developed turbulence, it has been proposed to relate the velocity-vorticity correlations to the mean vorticity gradient through
 540 a Boussinesq diffusion-like model (Tennekes and Lumley, 1972). In the present case, however, this kind of model does not predict the right sign for the mean vorticity flux.

5. Discussion and perspectives

A RNL system, for which a single streamwise Fourier mode is retained for the
 545 fluctuation, is used to identify laminar/turbulent transition paths that require the minimum energy. Using a Lagrangian formulation for the constrained RNL system, two types of initial perturbations can be considered. While the first set only involves the initial energy of the fluctuation, the second one uses a combination of the mean and the fluctuating parts. Only the first category is
 550 investigated in this study.

The same pCf case as the one studied by Duguet et al. (2013) is considered. We have identified two optimals, one for moderate target times and one for large target times. Both of them exhibit spanwise localization. While the first optimal appears symmetric with respect to the mid-plane $y = 0$, the second

555 optimal is non-symmetric. The dynamics in the physical space displays all the mechanisms identified in a fully nonlinear framework (Kerswell, 2018). For both optimals, mean streamwise vortices are generated from nonlinear interaction of three-dimensional oblique modes that get amplified through the Orr and lift-up mechanisms. At the earliest times, the generation of mean streamwise vortices is 560 dominated by the convective term. The mean streamwise vortices generate low- and high-speed streaks on both walls by lift-up effect. For the first optimal, streaks are symmetric with respect to the mid-plane $y = 0$. For the second one, the streak near the upper wall develops more rapidly than the one near the lower wall in the early stages. Turbulence first develops locally, before spreading 565 in spanwise direction. We show that all mechanisms are quantitatively well approximated by the RNL model.

From a geometrical viewpoint, both trajectories appear to approach an edge state. The edge state for the first optimal shows symmetry with respect to the channel mid-plane and exhibits strong similarities with the class of spanwise- 570 localized invariant solutions given by Gibson and Brand (2014). However, further investigations are needed in order to draw firm conclusions. For the second optimal, the symmetry breaking leads the flow structure to evolve near a different edge state. It consists of an isolated high-speed streak sandwiched between two low-speed streaks. This restricted nonlinear optimal and the minimal seed 575 investigated by Monokrousos et al. (2011); Rabin et al. (2012); Duguet et al. (2013) for the same computational box and the same Reynolds numbers show numerous similarities. The minimal seed is characterized by a pattern oriented in a direction pointing against the shear inside a three-dimensionally localized region (in all directions). Apart from the fact that the RNL optimal obtained for 580 a large target time is extended in the streamwise direction, the non-symmetric RNL optimal is also localized in spanwise and wall normal directions. For the corresponding time evolving flow, both trajectories pass close to a similar spanwise-localized edge state. Furthermore, the routes to turbulence present the same known mechanisms: Orr mechanism, oblique wave interaction, lift-up, 585 streak secondary instability, streak breakdown, and spanwise spreading, that are

found to occur one after the other. Notably, the threshold energy found using RNL optimizations is only twice the one found using the full DNS. In particular, the scaling law obtained by RNL optimizations is quite similar to the one associated with the minimal seed ($O(Re^{-2.65})$) to be compared with $O(Re^{-2.7})$). For the true nonlinear optimal found by Duguet et al. (2013), the perturbation at the initial time is mainly driven by oblique wave interaction associated with the fundamental streamwise Fourier mode and harmonics. The RNL approximation prevents any contribution of harmonics. This major difference may explain the change in the kinetic energy threshold. Further work is then required to include harmonics using RNL systems. This issue is currently under investigation.

This work was granted access to the HPC resources of the FLMSN, “Fédération Lyonnaise de Modélisation et Sciences Numériques”, partner of EQUIPEX EQUIP@MESO.

Appendix A. Optimisation. Adjoint system.

As in the approaches of Biau and Bottaro (2009); Olvera and Kerswell (2017), the equations governing the optimal RNL system solution are deduced from the condition of extremality of the constrained Lagrangian (7). We recover equations (3), (4) and their adjoint counterparts:

$$\begin{aligned}
 -A_t &= Re^{-1}(A_{yy} + A_{zz}) + \mathcal{G}_A \\
 -B_t + A(U_b + U)_y + BV_y + CW_y &= -\Pi_y + Re^{-1}(B_{yy} + B_{zz}) \quad (\text{A.1})
 \end{aligned}$$

$$-C_t + AU_z + BV_z + CW_z = -\Pi_z + Re^{-1}(C_{yy} + C_{zz}),$$

$$-\hat{a}_t - i\alpha\hat{a}U_b - V\hat{a}_y - W\hat{a}_z = -i\alpha\hat{\pi} + Re^{-1}(-\alpha^2\hat{a} + \hat{a}_{yy} + \hat{a}_{zz}) + g_a$$

$$-\hat{b}_t - i\alpha\hat{b}U_b + \hat{a}U_{by} - Vb_y - Wb_z = -\hat{\pi}_y + Re^{-1}(-\alpha^2\hat{b} + \hat{b}_{yy} + b_{zz}) + g_b$$

$$-\hat{c}_t - i\alpha\hat{c}U_b - V\hat{c}_y - W\hat{c}_z = -\hat{\pi}_z + Re^{-1}(-\alpha^2\hat{c} + \hat{c}_{yy} + \hat{c}_{zz}) + g_c \quad (\text{A.2})$$

with the following notations

$$\mathcal{G}_A = i\alpha \left(\hat{a}\hat{u}^* + \hat{a}^*\hat{u} + \hat{b}\hat{v}^* + \hat{b}^*\hat{v} + \hat{c}\hat{w}^* + \hat{c}^*\hat{w} \right) + (\hat{a}\hat{v}^* + \hat{a}^*\hat{v})_y + (\hat{a}\hat{w}^* + \hat{a}^*\hat{w})_z$$

$$g_a = \tilde{v}A_y + \tilde{w}A_z, \quad g_b = \tilde{v}B_y + \tilde{w}B_z \quad \text{and} \quad g_c = \tilde{v}C_y + \tilde{w}C_z.$$

Note that the function \mathcal{G}_A characterizes the sensitivity to variations in the base flow (Marquet et al., 2008) and the functions g_a , g_b and g_c are associated with variations in the perturbation (Biau and Bottaro, 2009). Temporal initial and end conditions close the system of equations:

$$\mathbf{a}(T) = \tilde{\mathbf{u}}(T), \quad \mathbf{A}(T) = \mathbf{U}(T),$$

$$\zeta \tilde{\mathbf{u}}(0) = \mathbf{a}(0), \quad \lambda \mathbf{U}(0) = \mathbf{A}(0).$$

References

- 600 Alizard, F., 2015. Linear stability of optimal streaks in the log-layer of turbulent channel flows. *Physics of Fluids* 27, 105103.
- Alizard, F., 2017. Invariant solutions in a channel flow using a minimal restricted nonlinear model. *C.R. Mécanique* 345, 117–124.
- Alizard, F., Biau, D., 2019. Restricted nonlinear model for high- and low-drag events in plane channel flow. *J. Fluid Mech.* 864, 221–243.
- 605 Andersson, P., Brandt, L., Bottaro, A., Henningson, D.S., 2001. On the breakdown of boundary layer streaks. *J. Fluid Mech.* 428, 29–60.
- Asai, M., Minagawa, M., Nishioka, M., 2002. The instability and breakdown of a near-wall low-speed streak. *J. Fluid Mech.* 455, 289–314.
- 610 Beaume, C., Chini, G., Julien, K., Knobloch, E., 2015. Reduced description of exact coherent states in parallel shear flows. *Phys. Rev. E* 91(4), 043010.
- Beaume, C., Knobloch, E., Chini, G., Julien, K., 2014. Exact coherent structures in an asymptotically reduced description of parallel shear flows. *Fluid Dynamics Research* 47(1), 015504.

- 615 Benney, D., 1984. The evolution of disturbances in shear flows at high Reynolds numbers. *Stud. Appl. Math.* 70, 1–19.
- Biau, D., Bottaro, A., 2009. An optimal path to transition in a duct. *Phil. Transact. Royal Soc.* 367, 529–544.
- Blackburn, H.M., Hall, P., Sherwin, S.J., 2013. Lower branch equilibria in
620 Couette flow: the emergence of canonical states for arbitrary shear flows. *J. Fluid Mech.* 726, R2.
- Bottin, S., Dauchot, O., Daviaud, F., 1997. Intermittency in a locally forced plane Couette flow. *Phys. Rev. Lett.* 79, 4377–4380.
- Brandt, L., 2007. Numerical studies of the instability and breakdown of a
625 boundary-layer low-speed streak. *Eur. J. Mech. B/Fluids* 26, 64–82.
- Brandt, L., 2014. The lift-up effect: the linear mechanism behind transition and turbulence in shear flows. *Eur. J. Mech. B/Fluids* 47, 80–96.
- Brethiem, J., Meneveau, C., Gayme, D., 2015. Standard logarithmic mean velocity distribution in a band-limited restricted nonlinear model of turbulent
630 flow in a half-channel. *Physics of Fluids* 27, 011702.
- Brethiem, J., Meneveau, C., Gayme, D., 2018. A restricted nonlinear large eddy simulation model for high Reynolds number flows. *J. of Turbulence* 19, 141–166.
- Buffat, M., Le Penven, L., Cadiou, A., 2011. An efficient spectral method based
635 on an orthogonal decomposition of the velocity for transition analysis in wall bounded flow. *Computers & Fluids* 42, 62–72.
- Butler, K., Farrell, B., 1992. Three-dimensional optimal perturbations in viscous shear flow. *Physics of Fluids* 4, 1637–1650.
- Cherubini, S., De Palma, P., 2013. Nonlinear optimal perturbations in a Couette
640 flow: bursting and transition. *J. Fluid Mech.* 716, 251–279.

- Cherubini, S., De Palma, P., 2014. Minimal perturbations approaching the edge of chaos in a Couette flow. *Fluid Dynamics Research* 46, 041403.
- Cherubini, S., De Palma, P., 2015. Minimal-energy perturbations rapidly approaching the edge state in Couette flow. *J. Fluid Mech.* 764, 572–598.
- 645 Cherubini, S., De Palma, P., Robinet, J.C., 2015. Nonlinear optimals in the asymptotic suction boundary layer: transition thresholds and symmetry breaking. *Physics of Fluids* 27, 034108.
- Clever, R., Busse, F., 1997. Tertiary and quaternary solutions for plane Couette flow. *J. Fluid Mech.* 344, 137–153.
- 650 Cossu, C., Brandt, L., Bagheri, S., Henningson, D., 2011. Secondary threshold amplitudes for sinuous streak breakdown. *Physics of Fluids* 23, 074103.
- Deguchi, K., 2015. Self-sustained states at Kolmogorov microscale. *J. Fluid Mech.* 781, R6.
- Deguchi, K., Hall, P., Watson, A., 2013. The emergence of localized vortex-wave 655 interaction states in plane Couette flow. *J. Fluid Mech.* 721, 58–85.
- Duguet, Y., Brandt, L., Larson, B., 2010. Towards minimal perturbations in transitional plane Couette flow. *Phys. Rev. E* 82, 026316.
- Duguet, Y., Monokrousos, A., Brandt, L., 2013. Minimal transition thresholds in plane Couette flow. *Physics of Fluids* 25, 084103.
- 660 Duguet, Y., Schlatter, P., Henningson, D., 2009. Localized edge states in plane Couette flow. *Physics of Fluids* 21, 111701.
- Duguet, Y., Willis, A., Kerswell, R., 2008. Transition in pipe flow: the saddle structure on the boundary of turbulence. *J. Fluid Mech.* 613, 255–274.
- Farano, M., Cherubini, S., De Palma, P., Robinet, J.C., 2016. Subcritical transition scenarios via linear and nonlinear localized optimal perturbations in 665 plane Poiseuille flow. *Fluid Dynamics Research* 48, 061409.

- Farrell, B., Gayme, D., Ioannou, P., 2017. A statistical state dynamics approach to wall-turbulence. *Phil. Trans. R. Soc. A* 375, 20160081.
- Farrell, B.F., Ioannou, P.J., 2012. Dynamics of streamwise rolls and streaks in turbulent wall-bounded shear flow. *J. Fluid Mech.* 708, 149196.
- Gessner, F., 1973. The origin of secondary flow in turbulent flow along a corner. *J. Fluid Mech.* 58, 1–25.
- Gibson, J.F., Brand, E., 2014. Spanwise-localized solutions of planar shear flows. *J. Fluid Mech.* 745, 25–61.
- Hack, M.J.P., Zaki, T.A., 2014. Streak instabilities in boundary layers beneath free-stream turbulence. *J. Fluid Mech.* 741, 280–315.
- Hall, P., Sherwin, S., 2010. Streamwise vortices in shear flows: harbingers of transition and the skeleton of coherent structures. *J. Fluid Mech.* 661, 178205.
- Hall, P., Smith, F., 1991. On strongly nonlinear vortex/wave interactions in boundary-layer transition. *J. Fluid Mech.* 227, 641–666.
- Hamilton, J.M., Kim, J., Waleffe, F., 1995. Regeneration mechanisms of near-wall turbulence structures. *J. Fluid Mech.* 287, 317–348.
- Itano, T., Toh, S., 2001. The Dynamics of Bursting Process in Wall Turbulence. *J. of the Phys. Soc. of Japan* 70, 703–716.
- Jiménez, J., Moin, P., 1991. The minimal flow unit in near-wall turbulence. *J. Fluid Mech.* 225, 213240.
- Joseph, D.D., 1976. *Stability of Fluid Motions I*. Springer.
- Karp, M., Cohen, J., 2014. Tracking stages of transition in Couette flow analytically. *J. Fluid Mech.* 748, 896–931.
- Karp, M., Cohen, J., 2017. On the secondary instabilities of transient growth in Couette flow. *J. Fluid Mech.* 813, 528–557.

- Kerswell, R.R., 2018. Nonlinear nonmodal stability theory. *Annual Review of Fluid Mechanics* 50, 319–345.
- Khapko, T., Kreilos, T., Schlatter, P., Duguet, Y., Eckhardt, B., Henningson, D., 2016. Edge states as mediators of bypass transition in boundary-layer flows. *J. Fluid Mech.* 801, R2.
- Kim, J., 2011. Physics and control of wall turbulence for drag reduction. *Phil. Trans. R. Soc. A* 369, 1396–1411.
- Klebanoff, P., 1971. Effect of freestream turbulence on the laminar boundary layer. *Bull. Am. Phys. Soc.* 16, 1323.
- Landhal, M., 1980. A note on an algebraic instability of inviscid parallel shear flow. *J. Fluid Mech.* 98, 243–251.
- Marquet, O., Sipp, D., Jacquin, L., 2008. Sensitivity analysis and passive control of cylinder flow. *J. Fluid Mech.* 615, 221–252.
- Monokrousos, A., Bottaro, A., Brandt, L., Di Vita, A., Henningson, D.S., 2011. Nonequilibrium thermodynamics and the optimal path to turbulence in shear flows. *Phys. Rev. Lett.* 106, 134502.
- Nagata, M., 1990. Three-dimensional finite-amplitude solutions in plane Couette flow: bifurcation from infinity. *J. Fluid Mech.* 217, 519–527.
- Olvera, D., Kerswell, R.R., 2017. Optimizing energy growth as a tool for finding exact coherent structures. *Phys. Rev. Fluids* 2, 083902.
- Pausch, M., Yang, Q., Hwang, Y., Eckhardt, B., 2019. Quasilinear approximation for exact coherent states in parallel shear flows. *Fluid Dynamics Research* 51, 011402.
- Perkins, H., 1970. The formation of streamwise vorticity in turbulent flow. *J. Fluid Mech.* 44, 721–740.

- Pershin, A., Beaume, C., Schneider, T., 2019. Dynamics of spatially localized states in transitional plane Couette flow. *J. Fluid Mech.* 867, 414–437.
- Pralits, J.O., Bottaro, A., Cherubini, S., 2015. Weakly nonlinear optimal perturbations. *J. Fluid Mech.* 785, 135151.
- 720 Pringle, C., Kerswell, R., 2010. Using nonlinear transient growth to construct the minimal seed for shear flow turbulence. *Phys. Rev. Lett.* 105, 154502.
- Pringle, C., Willis, A., Kerswell, R.R., 2012. Minimal seeds for shear flow turbulence: using nonlinear transient growth to touch the edge of chaos. *J.*
- 725 *Fluid Mech.* 702, 415–443.
- Rabin, S.M.E., Caulfield, C.P., Kerswell, R., 2012. Triggering turbulence efficiently in plane Couette flow. *J. Fluid Mech.* 712, 244–272.
- Reddy, S., Schmid, P., Baggett, J., Henningson, D.S., 1998. On stability of streamwise streaks and transition thresholds in plane channel flows. *J. Fluid*
- 730 *Mech.* 365, 269–303.
- Rosenberg, K., McKeon, B., 2019. Computing exact coherent states in channels starting from the laminar profile: a resolvent-based approach. *Phys. Rev. E* 100, 021101(R).
- Schmid, P., Henningson, D., 2001. *Stability and Transition in Shear Flows.*
- 735 *Applied Mathematical Sciences* 142, Springer.
- Schneider, T., Marinc, D., Eckhardt, B., 2010. Localized edge states nucleate turbulence in extended plane Couette cells. *J. Fluid Mech.* 646, 441–451.
- Schoppa, W., Hussain, F., 2002. Coherent structure generation in near-wall turbulence. *J. Fluid Mech.* 453, 57–108.
- 740 Skufca, J.D., Yorke, J.A., Eckhardt, B., 2006. Edge of chaos in a parallel shear flow. *Phys. Rev. Lett.* 96, 174101.

- Swearingen, J., Blackwelder, R., 1987. The growth and breakdown of streamwise vortices in the presence of a wall. *J. Fluid Mech.* 182, 255–290.
- Tennekes, H., Lumley, J., 1972. *A First Course in Turbulence*. The MIT press.
- 745 Thomas, V., Farrell, B., Ioannou, P., Gayme, D., 2015. A minimal model of self-sustaining turbulence. *Physics of Fluids* 27, 105104.
- Vaughan, N.J., Zaki, T.A., 2011. Stability of zero-pressure-gradient boundary layer distorted by unsteady Klebanoff streaks. *J. Fluid Mech.* 681, 116–153.
- Viswanath, D., Cvitanovic, P., 2009. Stable manifolds and the transition to
750 turbulence in pipe flow. *J. Fluid Mech.* 627, 215–233.
- Waleffe, F., 1998. Three-dimensional coherent states in plane shear flows. *Phys. Rev. Lett.* 81, 4140–4143.
- Waleffe, F., 2003. Homotopy of exact coherent structures in plane shear flows. *Physics of Fluids* 15, 1517–1534.
- 755 Waleffe, F., Kim, J., 1997. How streamwise rolls and streaks self-sustain in a shear flow. *Computational Mechanics Publications R. Panton, Ed.* , 309–332.
- Wang, J., Gibson, J., Waleffe, F., 2007. Lower Branch Coherent States in Shear Flows: Transition and Control. *Phys. Rev. Lett.* 98, 204501.